Published in final edited form as:
J Am Chem Soc. 2021 October 06; 143(39): 16007–16029. doi:10.1021/jacs.1c05436.

Nuclear Resonance Vibrational Spectroscopic (NRVS) Definition of the Fe(IV)$_2$ Intermediate Q in Methane Monooxygenase and its Reactivity

Ariel B. Jacobs[a], **Rahul Banerjee**[b], **Dory E. Deweese**[a], **Augustin Braun**[a], **Jeffrey T. Babicz Jr.**[a], **Leland B. Gee**[a], **Kyle D. Sutherlin**[a], **Lars H. Böttger**[a], **Yoshitaka Yoda**[c], **Makina Saito**[d], **Shinji Kitao**[e], **Yasuhiro Kobayashi**[e], **Makoto Seto**[e], **Kenji Tamasaku**[f], **John D. Lipscomb**[b], **Kiyoung Park**[g], **Edward I. Solomon**[a,h]

[a]Department of Chemistry, Stanford University, 333 Campus Drive, Stanford, California, 94305, United States

[b]Department of Biochemistry, Molecular Biology and Biophysics, University of Minnesota, Minneapolis, Minnesota 55391 U.S.A.

[c]Japan Synchrotron Radiation Research Institute, Hyogo 679-5198, Japan

[d]Department of Physics, Graduate School of Science, Tohoku University, Sendai, Miyagi 980-8578 Japan

[e]Institute for Integrated Radiation and Nuclear Science, Kyoto University, Osaka, 590-0494

[f]RIKEN SPring-8 Center, RIKEN, Sayo, Hyogo, 679-5148, Japan

[g]Department of Chemistry, Korea Advanced Institute of Science and Technology (KAIST), Daejeon 34141, Republic of Korea

[h]Stanford Synchrotron Radiation Light Source, SLAC National Accelerator Laboratory, Stanford University, Menlo Park, California, 94025, United States

Abstract

Methanotrophic bacteria utilize the non-heme diiron enzyme soluble methane monooxygenase (sMMO) to convert methane to methanol in the first step of their metabolic cycle under copper-limiting conditions. The structure of the sMMO Fe(IV)$_2$ intermediate Q responsible for activating the inert C-H bond of methane (BDE = 104 kcal/mol) remains controversial, with

---

Corresponding Authors John D. Lipscomb: Department of Biochemistry, Molecular Biology and Biophysics, University of Minnesota, Minneapolis, Minnesota 55391, U.S.A. lipsc001@umn.edu; Kiyoung Park: Department of Chemistry, Korea Advanced Institute of Science and Technology (KAIST), Daejeon 34141, Republic of Korea. kiyoung.park@kaist.ac.kr; Edward I. Solomon: Department of Chemistry, Stanford University, 333 Campus Drive, Stanford, California, 94305, United States. solomone@stanford.edu.

Supporting Information
Materials and Methods. Figures S1-S44 and Tables S1-S15. Additional data and figures including Mössbauer spectra speciation fits, decay of Q NRVS features over time, DFT model used for Q optimizations, DFT vibrational analysis, TD-DFT calibration, TD-DFT natural transition orbital (NTO) analyses, molecular orbital diagrams, additional TD-DFT calculated spectra, TD-DFT calculated linear coupling term (LCT) analyses, DFT correlation of B3LYP and BP86/10% HF functionals, DFT calculated NRVS spectra for cryoreduced Q models, DFT calculated NRVS spectra and structures for 90 Q models including predicted resonance Raman vibrational signals and Fe-Fe distances, reaction coordinate calculations for mononuclear, open core, and closed core Q models, and TD-DFT analysis of Q Fe-K-pre-edge region.

recent studies suggesting both "open" and "closed" core geometries for its active site. In this study, we employ nuclear resonance vibrational spectroscopy (NRVS) to probe the geometric and electronic structure of intermediate Q at cryogenic temperatures. These data demonstrate that Q decays rapidly during the NRVS experiment. Combining data from several years of measurements, we derive the NRVS vibrational features of intermediate Q as well as its cryoreduced decay product. A library of 90 open and closed core models of intermediate Q is generated using density functional theory (DFT) to analyze the NRVS data of Q and its cryoreduced product, as well as prior spectroscopic data on Q. Our analysis reveals that a subset of closed core models reproduce these newly acquired NRVS data as well as prior data. The reaction coordinate with methane is also evaluated using both closed and open core models of Q. These studies show that the potent reactivity of Q towards methane resides in the "spectator oxo" of its Fe(IV)$_2$O$_2$ core, in contrast to non-heme mononuclear Fe(IV)=O enzyme intermediates that H-atom abstract from weaker C-H bonds.

Graphical Abstract

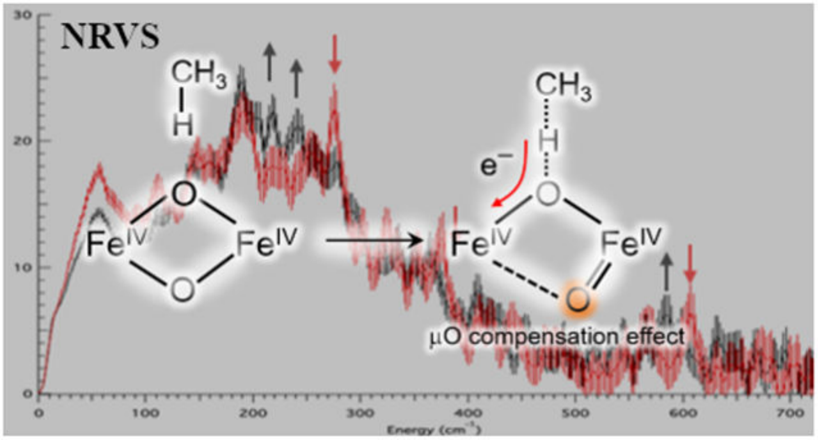

1. Introduction

The superfamily of binuclear non-heme (NH2Fe) enzymes[1] plays major roles in all realms of life including metabolism,[2-3] biotechnology,[4-5] drug design,[6-7] and bioremediation.[8] They share in common an active site composed of histidine and carboxylate residues that house the binuclear iron core. The reductive activation of dioxygen by this cofactor initiates a wide range of chemistries with substrates including N-oxygenation,[9] electrophilic aromatic substitution (EAS), [10] and hydroxylation.[11-12] Spectroscopic studies of O$_2$-activated intermediates in several NH2Fe enzymes have led to an improved understanding of their reaction mechanisms.[13-14]

Under low [Cu] conditions, methanotrophic bacteria utilize the NH2Fe enzyme soluble methane monooxygenase (sMMO) to convert methane to methanol in the first step of its metabolic cycle.[15,16] The quaternary structure of this enzyme complex consists of three component subunits: a hydroxylase $(\alpha\beta\gamma)_2$ (MMOH), which holds the NH2Fe cofactor; an electron transfer reductase (MMOR) that supplies two electrons to the NH2Fe cofactor during catalysis; and a regulatory component (MMOB) that binds to MMOH, greatly enhancing its product yield, O_2 reactivity, and turnover frequency.[17-20] To produce methanol, this enzyme complex must activate the inert C-H bond of methane (BDE = 104 kcal mol^{-1}) at ambient conditions, a chemical feat otherwise unprecedented in iron enzymology. The catalytic cycle of sMMO has been intensely studied under single-turnover conditions, leading to the identification of several intermediates including the methane-reactive intermediate Q.[19-23] Mössbauer spectroscopy has defined intermediate Q as having a high-spin, antiferromagnetically-coupled $Fe(IV)_2$ electronic structure.[24] This intermediate stands alone in the NH2Fe superfamily, for which most other substrate-reactive intermediates to date have been characterized as biferric (hydro)peroxides[13] (and in some cases ferric superoxide).[25,26]

The structure of intermediate Q was originally assigned in the late 1990s as a closed "diamond" $Fe_2(\mu\text{-}O)_2$ core from extended X-ray absorption fine structure (EXAFS) data[27] indicating a short Fe-Fe distance of 2.46 Å. This assignment was supported by a more recent (2015) continuous flow resonance Raman (rR) study,[28] which revealed a 690 cm^{-1} vibration showing $^{18}O_2$ and $^{16}O^{18}O$ isotopic shifts consistent with the vibrational spectra of diamond core model complexes[29,30] and O_2 loading into the Fe_2O_2 core. An additional peak at 556 cm^{-1} observed upon the decay of Q in this study also showed an $^{18}O_2$ (but no unique $^{16}O^{18}O$) shift, and was assigned to an $Fe(III)_2$ mono-μ-O species formed after methanol production (with loss of one labeled oxygen to methanol). Kinetic studies of the reaction of intermediate Q with methane reported a low activation barrier[31] ($\Delta G^{\ddagger}$ = 10 kcal mol^{-1} at 4 °C) and large deuterium kinetic isotope effect[32] (KIE = 50), indicating an H-atom abstraction from the strong C-H bond of CH_4. These EXAFS and reaction kinetics studies prompted a number of theoretical investigations into the reactivity of methane hydroxylation by closed core Q models.[33-39] Various closed core models have been proposed, including a Fe_2O_2 diamond core with one[33] or two μ-1,3-carboxylate bridges,[31] and with or without an exogenous water ligand.[30] Irrespective of the proposed model, all candidate structures optimized with a high-spin electronic structure resulted in Fe-Fe distances of ≥ 2.65 Å, far longer than measured by EXAFS.

In 2010, a high-spin "open" core O=Fe(IV)—O—Fe(III)—OH model complex was reported that exhibited a second order rate constant for dihydroanthracene oxidation 10^6 higher than its low-spin diamond core precursor.[40,41] This observation fueled speculation into the possibility of an open core assignment for Q. Since this report, two studies using high-energy resolution fluorescence detected (HERFD) X-ray absorption spectroscopy (XAS) on rapid freeze-quenched (RFQ) samples of Q have advocated for the possibility of an open core assignment. First, an analysis of the high intensity of the HERFD-XAS pre-edge region of the Q spectrum showed that the pre-edge was best reproduced by an open core model complex possessing a terminal oxo; this high pre-edge intensity of Q was alternatively not reproduced by a Fe_2O_2 diamond core model complex.[42] Second, remeasurement of the EXAFS region using HERFD-XAS did not reproduce the Fe-Fe 2.46 Å scatterer, which was determined to be a background metallic iron contribution.[43] The new RFQ-Q HERFD-EXAFS data were fit with an Fe-Fe distance of 3.30-3.34 Å, longer than the 3.27 Å distance of the ~ 50-60% $Fe(II)_2$ species ($MMOH_{red}$) also present in the RFQ-Q sample. This finding was interpreted as Q possessing a longer Fe-Fe distance (3.4 Å) than $MMOH_{red}$, which required an open core structural assignment. Though these studies have cast doubt on the closed core assignment of Q, no general consensus has been reached on its geometric structure and therefore the relevance of past calculations on closed core models.

Defining the geometric structure of Q thus requires further spectroscopic insight. The continuous-flow rR feature at 690 cm^{-1} informs on the mechanical coupling of O_2 incorporated atoms, but this feature alone provides limited structural insight. However, the ^{57}Fe preparations of sMMO used for RFQ-Mössbauer spectroscopy also enable the use of nuclear resonance vibrational spectroscopy (NRVS). This technique probes the vibrational sidebands in the ^{57}Fe nuclear Mössbauer transition and reports on all vibrations with significant ^{57}Fe displacement.[44-46] NRVS studies by our group have successfully characterized high-valent oxygen intermediates in binuclear[47] and mononuclear enzymes[48] and their models,[49,50] as well as iron-containing zeolites.[51] In the present study we utilize NRVS to study RFQ samples of Q. This hot intermediate is found to rapidly decay in the beam. Scanning multiple samples of Q over several years of experiments has enabled the separation of the Q NRVS spectrum from its decay. Further, the decay of Q in the X-ray beam is found to involve its cryoreduction; thus the NRVS spectrum of Q decay provides a spectral perturbation to assist in the assignment of Q. DFT calculations have been used to generate 90 structural models to correlate to the Q NRVS data as well as to prior spectroscopic data. This study yields deeper insight into the structure of Q as well as its reactivity relative to mononuclear non-heme iron enzymes.

2. Results

2.1. NR VS of Intermediate Q

Intermediate Q is formed by reaction O_2 with biferrous MMOH in complex with equimolar (vs MMOH active sites) MMOB. Thus, all samples analyzed here contain a complex of MMOH and MMOB. NRVS data collected on RFQ-Q samples measured at BL09XU exhibit time-dependent changes in the beam at cryogenic temperatures. The NRVS spectrum of a high-purity preparation of Q (50% of total iron, 37% biferrous ($MMOH_{red}$), 13% biferric ($MMOH_{ox}$); see Figure S1 for quantitation) displays an intense feature at 275 cm^{-1} in the first 10 scans (1 hour/scan) which disappears after 20 total scans (Figure S2, bottom to top). Concomitant with the decay of the 275 cm^{-1} feature is the growth of intensity between 200-250 cm^{-1} during 40 hours of measurement. Other RFQ samples of Q containing a lower quantity of Q (40%) and higher $MMOH_{red}$ (50%) also exhibited weaker intensity at 275 cm^{-1} that goes away with increasing scans. Therefore, in order to clearly distinguish the NRVS features of Q (early time data) and its decay product (late time points), seven samples of Q were measured up to 80 hours (ranging from 20 to 80 hours per sample). Binning sixty scans from these samples into ten-hour windows demonstrates biphasic, time-dependent NRVS changes (Figure S3, bottom to top): in the first phase, the 275 cm^{-1} feature and a weaker (but reproducible above noise) feature at 605 cm^{-1} decay and are no longer present after 20 hours of measurement (bottom to middle, black arrows), while features between 220-240 and at 580 cm^{-1} grow in (middle, red arrows). In the second decay phase, the 220-240 and 580 features continue to increase in intensity and no longer change after 30 hours of measurement (top, black arrows). The decay of a 375 cm^{-1} feature is also observed in these phases (top, black line), resulting in a local maximum in the late time point NRVS data at 365 cm^{-1}. NRVS data combined from several samples into sets of 5-hour intervals (Figure S4) corroborate the decay of the 605 and 275 cm^{-1} features, and the growth of the 220, 240, and 580 cm^{-1} features within the first 15 hours of measurement (first phase). Final early and late time scan Q NRVS data were generated by compiling over one-hundred scans between 1-15 and 30-80 hours of measurement, and these are shown in Figure 1A top as red and black, respectively. Additionally shown in Figure 1A top (orange) is the NRVS spectrum of a $MMOH_{red}$ sample which was scaled down to reflect the 50% $Fe(II)_2$ present in the “Q” sample. Subtraction of 50% $MMOH_{red}$ and renormalization generates the spectra at the bottom of Figure 1A for the Q (red) and Q decay (black) NRVS data. The overlay of these spectra confirms that the time-dependent changes observed between early and late Q NRVS data (red down arrows and up black arrows, respectively) are outside of noise, as are additional features at 420, 330, and 300 cm^{-1} which do not change between the early and late Q NRVS data (lighter coincident red and black lines). Thus, NRVS data of Q reveal strong time-dependent changes in the beam at both low (200-400 cm^{-1}) and high (560-610 cm^{-1}) energies. The early time data define the NRVS features of intermediate Q, and the late time data provide the NRVS spectrum of its decayed features in the X-ray beam.

In addition, intermediate Q samples were also prepared with $^{18}O_2$. While the $^{16}O_2$ Q samples could be generated using chlorite dismutase and were thus concentrated enough to display significant NRVS intensities in the early scans, the $^{18}O_2$ samples had to be prepared with $^{18}O_2$-saturated buffer and thus were more dilute (1.00 mM total iron vs. 1.80 mM). The $^{18}O_2$ generated Q samples required more accumulation time for good S/N and isotope perturbations could only be obtained for the late time (30-80 hour) decay data. Two isotope shifts are observed in the decayed Q NRVS spectrum: a 12-15 cm^{-1} downshift of the 420 cm^{-1} feature, and a small downshift of the 580 cm^{-1} feature (Figure 1B; see Figure S5 for raw data counts in this region). While limited by the S/N of ~ 2, analysis of the 580 cm^{-1} feature (Figure S6) reveals an isotope shift of 4–7 cm^{-1}.

In summary, Q shows NRVS peaks at 605, 420, 375, 330, 300, and 275 cm^{-1}. The decay of Q results in the loss of the 605, 375, and 275 cm^{-1} features and produces new peaks at 580, 365, 240, and 220 cm^{-1}. The features at 580 and 420 cm^{-1} in the decayed Q spectrum show a $^{16}O/^{18}O$ effect of 4-7 cm^{-1} and 12-15 cm^{-1}, respectively.

2.2. Mössbauer of Q NRVS Samples and Parallel Data On Cryoreduced Q

It was hypothesized that the decay of Q in the X-ray beam during NRVS data collection was due to its photoreduction. Mössbauer spectra were obtained on RFQ Q samples before and after NRVS experiments to quantify the amount of Q decay and identify any new species formed due to photoreduction. To track the decay of Q during NRVS measurements, parallel experiments were performed on frozen-solution Q samples at BL19LXU at SPring-8. Samples measured at BL19LXU were prepared in 11 x 4 x 1.2 mm rectangular holders; illumination of these samples results in an estimated 25% total volume exposure to the NRVS X-ray beam. The NRVS spectrum of a BL19LXU Q sample after 14 hours overlays well with the NRVS spectrum of BL09XU Q decay (Figure S7; due to the 3 times higher flux at BL19LXU). Importantly, The Mössbauer spectrum of the BL19LXU sample (Figure 2A red, speciation prior to NRVS experiment given in Figure S8) after NRVS measurement at BL19 for 14 hours shows two changes: 1) 20% reduction of the original Q in the full sample volume (Figure 2A, black, arrows pointing up at 0.50 mm/s and −0.14 mm/s where the second component of the Q doublet is located); and 2) concomitant growth of a new species with $\delta \approx 0.6$ and $\Delta E_Q \approx 1.60$ mm/s (Figure 2A, arrows pointing down at 1.45 mm/s and −0.14 mm/s; note the downward arrow at −0.14 mm/s reflects a compensating increase in signal for the loss of Q at this velocity) indicative of the formation of a ferric species and possibly photoreduction of the NRVS sample.

In order to evaluate whether the new ferric species in Figure 2A (downward arrows) is a product of Q photoreduction, samples of Q were independently cryoreduced using 6 Mrad of γ-ray emission from a radioactive ^{60}Co source. Similar experiments were reported by Valentine et al. on MMOH Q isolated from *Methylococcus capsulatus* (*Mc* Bath);[52] however, Mössbauer data have not yet been reported for cryoreduced Q from *Methylosinus trichosporium* OB3b (*Mt* OB3b) MMOH. Mössbauer spectra of Q before (Figure 2B top) and after cryoreduction revealed formation of a ferric species (Figure 2B, middle, arrow) with a feature at 1.45 mm/s, similar to the signal observed in the post-NRVS Mössbauer spectrum (Figure 2A, black), confirming cryoreduction of the NRVS sample. Application of a 73 mT parallel magnetic field resulted in no change of the 1.45 mm/s signal indicating it is a coupled biferric species, and revealed additional features at $\delta = -3.7, -1.7$, and 4.8 mm/s (Figure 2B, bottom, arrows), indicating the presence of a paramagnetic Fe(III)Fe(IV) species, similar to intermediate X[52,53] (here labeled Qx) in ribonucleotide reductase. Subtracting the $Fe(II)_2$, an initial $Fe(III)_2$ component present in Q before cryoreduction, and the Fe(III)Fe(IV) species from the bottom spectrum in Figure 2B yields the diamagnetic biferric species (Q3; Figure S9, bottom), consisting of two inequivalent high-spin Fe(III) sites ($\delta_1 = 0.50$ mm/s, $\Delta E_{Q1} = 1.99$ mm/s; $\delta_2 = 0.63$, mm/s $\Delta E_{Q2} = 1.33$ mm/s) of equal intensity. Thus, the loss of the Q Mössbauer signal at 0.50 mm/s (Figure 2A) and the formation of a new ferric signal in the post-NRVS Mössbauer spectrum at −0.14 and 1.45 mm/s can be attributed to photoreduction of Q and formation of a high-spin antiferromagnetically coupled biferric decay product (through the mixed valent Qx). From simulating the BL19 post-NRVS Mössbauer spectrum (Figure S10), all of Q in the BL19 NRVS sample has decayed, leaving a mixture of Qx and Q3 (roughly 40%:60%). While the ratio of these two reduced species would vary with beam exposure, Qx and Q3 are calculated to have (*vide infra*) and do exhibit similar NRVS features (scan dependence in Figure S3). Thus, this variable is not an issue in the analysis of the NRVS decay spectra in Section 3.4.

3. Analysis

3.1. Structural Models for Intermediate Q

To determine possible structures for Q which best reproduce the NRVS and prior spectroscopic data, a library of 90 DFT models (Table S1) that contain two antiferromagnetically-coupled high-spin Fe(IV) centers was constructed by modifying the X-ray crystal structure of MMOB-associated MMOH from *Methylococcus capsulatus* (Bath. PDB 4GAM).[54] Though these crystals appear to have cryoreduced in the X-ray beam, a crystal structure of oxidized MMOH (without MMOB bound, PDB 1MHY) possesses three oxygen ligands, two $O(H)_x$ bridges and one terminal $O(H)_y$ moiety.[55] Therefore, a model with two (μ-O) bridges and a terminal H_2O (**bis(μO)-H_2O-1**) was chosen to preserve charge neutrality of the Q $Fe(IV)_2$ active site and served as a starting structural scaffold for optimization of Q models. This model choice has been justified by the recent report of the higher resolution crystal structure of fully oxidized MMOB-associated MMOH from *Methylosinus trichosporium* OB3b (see Section 3.4),[56] and has been further calibrated with DFT (Figure S11) for determination of the optimal truncation scheme.

The full library of Q models possesses either "closed core" structures with two $O(H)_x$ bridges (denoted bis(μO)-L-# in Table S1, where L is a terminal ligand to one Fe(IV)) or "open core" structures with one oxo bridge (denoted OC## in Table S1), with further variations in the protonation level of the carboxylate ligands and oxygenic terminal ligands including oxide, hydroxide, and water, and hydrogen bonding interactions. Closed core Q models with a terminal H_2O ligand (bis(μO)-H^2O subclass, 16 models) were initially constructed through ligand rearrangements of **bis(μO)-H_2O-1**. These models were further modified by deprotonating or removing the terminal H_2O ligand, resulting in bis(μO)-OH and bis(μO) subclasses (17 and 6 models, respectively) containing a variety of Glu coordination, conformation, and protonation states, as well as H-bonding interactions with the bis(μO) core or a non-coordinating H_2O molecule. Two other subclasses, (μOμOH) (8 models) and bis(μO)=O (4 models), are included in the SI and will be briefly presented. Representative bis(μO), bis(μO)-OH, and bis(μO)-H_2O structures are given at the bottom of Figure 3.

Open core models for Q were prepared by translocating a proton from the terminal water in **bis(μO)-H_2O-1** to a μ-O bridge and reoptimizing on the $Fe(IV)_2$ level. Opening of the core in this manner yielded a 5C square pyramidal and 6C site with a terminal OH^- trans-axial to a His. Models generated in this way with further variations in the conformations and H-bonds of the 1st-sphere Glu residues form the OH-Fe-O-Fe-OH (OC -OH/-OH) subclass. By either protonating or deprotonating the terminal OH^- ligand, 37 total open-core models were generated, including the OH-Fe-O-Fe=O (OC -OH/=O) subclass and three other open core subclasses, O=Fe-O-Fe=O (OC=O/=O), O=Fe-O-Fe-H_2O (OC -H_2O/=O), and OH-Fe-O-Fe-H_2O (OC -OH/-H_2O), to be presented in less detail (Table S1). Representative OC -OH/-OH and OC -OH/=O structures are given at the top of Figure 3.

3.2. Vibrational Analysis of Closed and Open Core Models of Q

The 90 possible models for intermediate Q generated in Section 3.1 were initially evaluated by computing their vibrational spectra using DFT methods (with the BP86 functional plus 10% HF) and comparing these results to the prior rR data on Q. This rR study[28] revealed that Q exhibits a vibration at 690 cm^{-1}, with a $^{18}O_2$ isotopic downshift of 36 cm^{-1} and a $^{16}O^{18}O$ mixed isotope downshift of 12-15 cm^{-1} (with no observable ^2H perturbation, for an experimental resolution of ~ 3 cm^{-1}). Furthermore, rR data of the methane-reacted product complex, T show a 556 cm^{-1} vibration with a $^{18}O_2$ downshift to 533 cm^{-1}, and two $^{16}O^{18}O$ mixed isotope signals at 556 and 533 cm^{-1} reflecting the presence a single labeled oxygen atom in T. These rR data on T define it as having a μ-O bridge derived from O_2. Therefore, these data together show that Q contains an O_2 derived core, with one of these oxygens loaded in a μ-O bridge. To screen candidates for Q from the library of 90 models, vibrational frequencies for $^{16}O_2$, $^{18}O_2$, $^{16}O^{18}O$, and ^2H isotopomers for each of the models were obtained from the DFT calculations and correlated to the experimental rR vibrational data ($^{16}O_2$ spectra for all models given in Table S1, along with tabulated $^{16}O^{18}O$, $^{18}O_2$ and ^2H perturbations).

Closed core Q models of the bis(μO), bis(μO)-OH, and bis(μO)-H_2O subclasses exhibit three modes above 600 cm^{-1}: a symmetric (A_g) breathing mode at 700 cm^{-1}, as well as two non-symmetric (B_{3u} and B_{2u}) modes (using effective D_{2h} symmetry for a Fe_2O_2 core) between 600 and 650 cm^{-1} (ν_1, ν_2, ν_3 in Figure 4 top, respectively). Incorporation of $^{18}O_2$ and $^{16}O^{18}O$ into the (μ-O)$_2$ core results in downshifts of the breathing mode by 30-40 cm^{-1} and 15-20 cm^{-1}, respectively. The absence of proton involvement in the breathing mode results in no predicted ^2H effect. The breathing mode of all bis(μO) models, as well as 12 out of 16 bis(μO)-H_2O models, reproduces the Q rR 690 cm^{-1} feature well (highlighted in red in Figure 4 top), and is similar to rR data collected on bis(μO) model complexes.[29,30] However, the symmetry of the Fe_2O_2 core mediates the degree of coupling between the (μ-O)$_2$ units. For example, in **bis(μO)-H_2O-16**, hydrogen bonding (heavy atom distance = 2.5 Å) between E144 and one (μ-O) introduces a C_{2v} distortion into the core (Fe_1-O_a = 1.83, Fe_2-O_a = 1.95 Å, Fe_1-O_b = 1.74, Fe_2-O_b = 1.85). As a result, **bis(μO)-H_2O-16** possesses two uncoupled ν(Fe_1-O_a) and ν(Fe_2-O_b) stretches above 600 cm^{-1} which localize onto the short Fe-O bonds, and prevents the appropriate mixed isotope shift in the $^{16}O^{18}O$ isotopomer (similar distortions are found in **bis(μO)-H_2O-5**, **7**, and **13**; see Table S1). In the bis(μO)-OH subclass, the strong ligand field of the terminal OH$^-$ produces a large C_{2h} distortion and uncoupling of the core vibrations (models **bis(μO)-OH 1-5**, **7, 9**, **17-18)**. In contrast to the bis(μO)-H_2O subclass, hydrogen bonding to the (μ-O)$_2$ unit in the bis(μO)-OH structures decreases the distortion. This increases the (μ-O)$_2$ mechanical coupling and results in a breathing mode vibration near 690 cm^{-1} with the appropriate mixed isotope shift. The influence of the OH$^-$ ligand is such that, of the remaining 9 bis(μO)-OH models (**bis(μO)-OH 6, 8, 10-16**) possessing a coupled A_g breathing mode, 7 of them contain a hydrogen bond to the (μ-O)$_2$ unit (models **bis(μO)-OH 6**, **10-14, 16)**. For all three bis(μO), bis(μO)-OH, and bis(μO)-H_2O subclasses, the 690 cm^{-1} vibration is well reproduced by a breathing mode in models without strong C_{2v} or C_{2h} distortions (i.e., in models for which all Fe-O bond lengths in the Fe_2O_2 core are similar)

The two other closed core Q subclasses, bis(μO)=O and (μOμOH), do not possess a feature above 600 cm^{-1} with an appropriate mixed isotope downshift. In bis(μO)=O models, the terminal oxo facilitates an opening of the core to a O=Fe-O-Fe=O structure; therefore, only one antisymmetric μ-O stretch (ν_{as}(Fe-O-Fe)) is observed between 600-740cm^{-1}. This is true as well for (μOμOH) models which lack a coupling of the μ-OH stretches to the ν_{as}(Fe-O-Fe) mode. Thus, these models do not predict the observed average mixed isotope downshift in the $^{16}O^{18}O$ isotopomer and are excluded from further consideration.

Though previous literature had identified closed core models as structural candidates for Q based on the 690 cm^{-1} vibration and $^{16}O^{18}O$ mixed isotope shift, an open question remains as to how an open core model as suggested by recent EXAFS data could reproduce these rR data. This question is now addressed. In Q open core models, the Fe-OH stretch (ν(Fe-OH)) and ν_{as}(Fe-O-Fe) appear between 600 and 750 cm^{-1}. If these vibrations occur close in energy, they mix to form symmetric (ν(Fe-OH) + ν_{as}(Fe-O-Fe)) and antisymmetric (ν(Fe-OH) − ν_{as}(Fe-O-Fe)) combinations (Figure 4, ν_1 and ν_2 middle row, and ν_2 and ν_3 bottom row).

For OC -OH/=O models possessing an OH-Fe_2-(μ-O)-Fe_1=O structure, The Fe_1=O bond weakens the Fe_1-(μ-O) bond resulting in a shorter Fe_2-(μ-O) bond, localizing ν_{as}(Fe-O-Fe) on the Fe_2 side. This facilitates ν(Fe-OH) + ν_{as}(Fe-O-Fe) coupling, resulting in a symmetric mode ν_2 which would agree with the 690 cm^{-1} experimental data (Figure 4, bottom row, red box), as anticipated in a recent computational study of Q.[57] Isotope labeling with $^{18}O_2$ must be incorporated into the μ-O bridge to correlate to the decay product T, as well as either into the -OH or =O terminal ligands. Incorporation of ^{18}O into the =O position does not lead to an observed mixed isotope signal, since the oxo vibration is too high in energy (800 cm^{-1}) to influence ν_2 (Figure S12). Therefore, the $^{18}O_2$ would have to be incorporated into the -OH and μ-O ligands. OC -OH/=O $^{18}O_2$ and $^{16}O^{18}O$ isotopomers display a downshift of ν_2 by 20-40 and 10-20 cm^{-1} (respectively), which reproduce the Q rR experimental data. Importantly, the mixed isotope signal strongly depends on the similarity between Fe_2-OH and Fe_2-(μ-O) bond lengths. Fe_2-OH and Fe_2-(μ-O) bond lengths differing by more than 0.05 Å results in the uncoupling of the ν(Fe-OH) and ν_{as}(Fe-O-Fe) vibrations and the absence of the appropriate mixed isotope shift (**OC2, OC22, OC24, OC25**). This ν(Fe-OH) + ν_{as}(Fe-O-Fe) mode coupling is also facilitated by hydrogen-bond donation to the Fe_1=O oxo, which weakens the Fe_1=O bond and strengthens the Fe_1-(μ-O) bond, resulting in elongation of the Fe_2-(μ-O) bond. Of the remaining OC -OH/=O models, **OC17** and **OC26** exhibit ν_2 matching the experimental 690 cm^{-1} vibration and its isotope shifts, facilitated by hydrogen-bond donation (from a glutamic acid or OH^-) to the terminal oxo. Note, however, that two of these models (**OC1** and **OC3**) exhibit ν_2 ^2H downshifts of 8 cm^{-1} that is too large based on the rR data; an explanation for this effect is provided below.

In OC -OH/-OH models, three vibrations appear between 600 and 750 cm^{-1}: two ν(Fe-OH) (denoted ν(Fe_1-OH) and ν(Fe_2-OH)) and one ν_{as}(Fe-O-Fe) vibration which may mix to give symmetric and antisymmetric combinations (Figure 4, middle). In these OH-Fe_1-(μ-O)-Fe_2-OH models, the Fe_1-OH vector is oriented out-of-plane with respect to the Fe-O-Fe plane and ν(Fe_1-OH) couples weakly with the ν(Fe_2-OH) and ν_{as}(Fe-O-Fe) vibrations. Thus two coupled modes are observed near 700 cm^{-1}: ν(Fe_2-OH) + ν_{as}(Fe-O-Fe) and ν(Fe_2-OH) − ν_{as}(Fe-O-Fe) (Figure 4, middle row, ν_1 and ν_2), as well as one uncoupled ν(Fe_1-OH) mode (ν_3). Hence, to reproduce the experimental isotope shifts the two atoms of $^{18}O_2$ must incorporate into the in-plane hydroxide (Fe_2-OH) and the μ-O ligands. For OC -OH/-OH models mode ν_1 exhibits $^{18}O_2$ and $^{16}O^{18}O$ isotopic shifts of 20-40 and 10-20 cm^{-1} (respectively), agreeing well with the experimental Q rR data. Due to the similarity of the Fe_2-OH and Fe_2-(μ-O) bond lengths (Δ = 0.02-0.03 Å), 13 out of 14 OC -OH/-OH models display ν_1 with a mixed isotope downshift of 10-20 cm^{-1}. However, 9 of these 13 models exhibit a large ν_1 downshift upon deuterium labeling ($|\Delta^2H| \geq 5$ cm^{-1} for **OC9**, **OC11**, **OC13**, **OC18**, **OC19**, **OC20**, **OC23**, **OC33**, **OC34**), as observed in the OC -OH/=O **OC1** and **OC3** models (*vide supra*). This is due to significant mixing of the OH torsional twist into the in-plane ν(Fe_2-OH) stretch; this torsion mode downshifts by more than 100 cm^{-1} upon ^{2}H labeling and hence downshifts ν(Fe_2-OH) (Figure S13). The remaining models (**OC10, OC15, OC16, OC32**) possess a ν_1 with a mixed isotope signal that reproduces the 690 cm^{-1} rR vibration well with no significant ^{2}H effect.

The remaining OC =O/=O, -H_2O/=O and -OH/-H2O subclasses do not exhibit a 690 cm^{-1} vibration with an appropriate mixed isotope downshift for the $^{16}O^{18}O$ isotopomer and are excluded from further consideration. Both OC =O/=O and OC -H_2O/=O subclasses display a single ν_{as}(Fe-O-Fe) vibration between 600-750 cm^{-1} with no coupling partner. In the OC -OH/-H_2O subclass, the Fe-(μ-O) bond on the OH- side is too long to permit ν(Fe-OH) and ν_{as}(Fe-O-Fe) coupling.

Thus, both closed core and open core Q models predict vibrations near 690 cm^{-1} with a $^{16}O^{18}O$ labeled mixed isotope shift that would correspond to the experimental rR data. The bis(μO), bis(μO)-OH, and bis(μO)-H_2O models display the canonical A_g breathing mode, which upon $^{16}O^{18}O$ labeling into the $(\mu\text{-O})_2$ core exhibits an appropriate mixed isotope shift. For OC -OH/=O models, the ν_{as}(Fe-O-Fe) mode localizes on the Fe_2-OH side and mixes with the ν(Fe_2-OH) vibration to produce a symmetric ν(Fe_2-OH) + ν_{as}(Fe-O-Fe) mode. Labeling of the OH- and μ-O ligands with $^{16}O^{18}O$ and $^{18}O_2$ would result in its downshift of 10-20 and 20-40 cm^{-1} respectively, which would agree well with experiment. The OC -OH/-OH subclass also exhibits a ν(Fe_2-OH) + ν_{as}(Fe-O-Fe) mode which agrees well with experiment, provided minimal rotation of the Fe_2-OH unit (that would result in a large deuterium isotope shift) and selective $^{18}O_2$ labeling of the in-plane Fe_2-OH and μ-O ligands. All calculated isotope perturbations are included in Table S1 for the 90 Q model library.

3.3. TD-DFT Correlations to Absorption and Excited State Distortions

Normal mode vibrations in both Q closed core (ν_1, Figure 4 top) and open core models (ν_1 and ν_2, Figure 4 middle and bottom) have been identified as candidates for the 690 cm^{-1} feature in its rR spectrum. The UV-vis absorption spectrum for Q exhibits an intense (ε = 10 $mM^{-1}cm^{-1}$) band at 350 nm (28,600 cm^{-1}; Figure 5A) which, when probed with a 351 nm (28,500 cm^{-1}) laser line, results in the resonance-enhancement of the characteristic 690 cm^{-1} vibration. The absorption spectrum additionally shows a weak feature at 800 nm (12,500 cm^{-1}; ε = 1.2 $mM^{-1}cm^{-1}$. Insert Figure 5A), as well as rising intensity between 15,000 and 28,000 cm^{-1} with a local maximum at 23,000 cm^{-1} (ε = 8 $mM^{-1}cm^{-1}$). To correlate the Q models identified in Section 3.2 to the experimental absorption spectrum and its associated rR data, there are two points of focus: 1) prediction of the absorption spectra for structural subtypes of Q and in particular the nature of the transitions in the 350 nm region; and 2) determination of the excited state distortions associated with the 350 nm transitions that would lead to resonance enhancement. Therefore, TD-DFT (using the CAM-B3LYP functional to obtain reasonable carboxylate charge transfer energies)[58] was employed to calculate and assign the absorption spectra of the Q models (identified in Section 3.2) and predict the excited state distortions associated with 351 nm excitation.

The TD-DFT calculated spectra for closed core and OC -OH/-OH and OC -OH/=O models are shown in Figure 5. The predicted electronic transitions for the three classes are similar and may be described together (see SI, Figures S14-24 and Tables S2-12 for a full description of the TD-DFT calculations and analysis). The weak feature at 12,500 cm^{-1}

in the experimental data (Figure 5A, inset) is predicted to consist of Fe(IV) *d-d* transitions (Figure 5B-D, insets). The rising intensity above 15,000 cm^{-1} in the experimental data (Figure 5A) may be described as LMCT transitions involving μ-O, oxo, and OH^- donation into the Fe(IV) *dσ* LUMO* orbitals (Figure 5B-D; the dσ* LUMOs are given in Figure S17, S20, and S23). Importantly, the TD-DFT calculations predict the third critical spectral region incorporating the 28,600 cm^{-1} experimental peak (Figure 5A) to contain LMCT transitions involving μ-O and OH^- donation into the Fe(IV) *dπ** orbitals (Figure 5B-D, numbered transitions; the dπ* orbitals are given in Figure S17, S20, and S23) that are highly localized in nature (Note that for the open core models, the acceptor orbitals reside on Fe_2 containing the in-plane OH^- ligand in the OC -OH/-OH subclass and the OH^- ligand in the OC -OH/=O subclass; for examples, see Tables S8 and S10). In the bis(μO), bis(μO)-H_2O, and bis(μO)-OH subclasses, the $(\mu\text{-O})_2 \rightarrow \text{Fe(IV)}_2$ *dπ** LMCT would result in an excited state with an elongation of all four Fe_2-$(\mu\text{-O})_2$ bonds and resonance enhancement of the A_g breathing mode (Figure 4, top), as observed in M_2O_2 (M = metal) systems.[29,30] This prediction based on past model studies was evaluated by using TD-DFT to calculate the linear coupling terms (LCT) for the different possible normal modes in the 650 – 750 cm^{-1} region, where a large slope in the LCT (i.e., a large change in excited state transition energy with distortion along a normal mode) for a given vibration indicates a large exited state distortion, and thus significant resonance enhancement in its Raman spectrum. As observed in Figure 5B (right), the LCT for the bis(μO)-L (L = OH^-, H_2O, or vacant axial position) in the symmetric breathing mode has a larger slope (relative to other modes) and is thus calculated to be the dominant resonance enhanced vibration. From extension to the OC -OH/-OH and OC -OH/=O subclasses, we find that the ν_1 mode in the former and the ν_2 mode in the latter (both at ~ 690 cm^{-1}) do have large LCT slopes (Figure 5C-D on right; relative to other modes in this region with small slopes) and are also predicted to have significant resonance enhancement. This derives from the assignments of the transitions in this region of the absorption spectrum as μ-O and $OH^- \rightarrow Fe_2$(IV) *dπ** LMCT (see Tables S8-9). This would result in significant elongations of both the Fe_2-OH and Fe_2-(μ-O) bonds that corresponds to a positive distortion along the ν_1 (OC -OH/-OH) and ν_2 (OC -OH/=O) modes. All three modes identified as candidates for the 690 cm^{-1} rR feature in the possible Q structural types are thus predicted to be resonance enhanced by excitation at 351 nm (28,500 cm^{-1}). Hence, the TD-DFT calculations herein reproduce findings from previous studies that demonstrate resonance enhancement of the A_g mode (at 690 cm^{-1}) in Fe_2-$(\mu\text{-O})_2$ closed core systems. Importantly, they also predict resonance enhancement of the symmetric ν_1 (OC -OH/OH) and ν_2 (OC -OH/=O) modes at 690 cm^{-1} in Q open core models upon excitation at 351 nm, which results in μ-O and OH^- donation into localized Fe_2(IV) *dπ** orbitals.

3.4. NRVS Structural and Spectral Assignment of Q

In the previous sections, a number of models with open and closed core motifs have been evaluated and a limited number have been identified as structural candidates for Q through a correlation of their predicted absorption and rR spectra to experimental data. The remaining models have OC -OH/=O and OC -OH/-OH cores, as well as bis(μO) cores with only glutamate, or OH^- and H_2O axial ligands. These models are now further appraised using NRVS. The results from the NRVS experiments in Section 2.1 define unique features for Q in its PVDOS spectrum at 605, 420, 375, 330, 300 and 275 cm^{-1} (Figure 1A, red spectrum). Decay of these features was observed in two sequential phases (Figure S3), corresponding to the cryoreductive formation of a one-electron reduced high-spin, mixed-valence, antiferromagnetically-coupled Fe(III)Fe(IV) species (Qx), followed by further reduction to an Fe(III)$_2$ species (Q3). In the first decay phase, the 605 cm^{-1} and 275 cm^{-1} features are eliminated, with concomitant intensity growing in between 560-580 cm^{-1} and 220-240 cm^{-1}. In the second decay phase, intensity between 560-580 cm^{-1} and 220-240 cm^{-1} continues to grow and reaches a maximum. A feature at 375 cm^{-1} in the early Q data also decays during the measurement. Hence, the final decay spectrum (Figure 1A, black), containing contributions from a mixture of Fe(III)Fe(IV) and Fe(III)$_2$ species, exhibits a feature between 560-580 cm^{-1}, and at 420, 365, 330, 300, 240, and 220 cm^{-1}. Furthermore, the NRVS spectrum for the $^{18}O_2$ Q decay sample (Figure 1B) exhibits an observable but modest (4 - 7 cm^{-1}) downshift relative to the $^{16}O_2$ 560 - 580 cm^{-1} feature, and shows a 12-15 cm^{-1} downshift of the $^{16}O_2$ 420 cm^{-1} feature.

In order to screen the possible candidates for Q using NRVS, the DFT-calculated NRVS spectra for all candidate Q models (90 total) were correlated to the NRVS experimental data (Figure 1A, bottom red spectrum). Models with calculated Q NRVS spectra that reproduce the experimental spectrum were then computationally "cryoreduced" for correlation to the cryoreduced-Q NRVS and Mössbauer data as a further screen. From Section 2.2, the NRVS sample at the end of the measurement contains 0% Q, 50% MMOH$_{red}$, and approximately 20% Fe(III)Fe(IV) (Qx) and 30% Fe(III)$_2$ (Q3) species. Therefore, calculated cryoreduced NRVS spectra were generated using 40% Fe(III)Fe(IV) and 60% Fe(III)$_2$ species (matching the speciation with MMOH$_{red}$ subtracted). Though this chosen component mixture is approximate, the calculations below and the experimental data in Figure S3 show that the NRVS features of Fe(III)Fe(IV) and Fe(III)$_2$ cryoreduced models are similar and therefore deviations from this composition would not significantly impact the calculated NRVS spectra. Two important considerations have been included in the generation of acceptable cryoreduced-Q models. First, in order to maximize the number of models possessing high-spin Fe(III)Fe(IV) and Fe(III)$_2$ electronic structures, cryoreduction-modeling calculations were performed with B3LYP which preferentially stabilizes high-spin states. The Fe(IV)$_2$ Q models obtained with 10% HF included with BP86 were reoptimized with B3LYP, which resulted in only minor changes in structures and vibrational profiles (spectra shown in Figure S25). These re-optimized Q structures were then used for cryoreduction modeling. Second, the cryoreduced-Q models were determined by fully optimizing the B3LYP Fe(IV)$_2$ Q models with high-spin Fe(III)Fe(IV)$_2$ and Fe(III)$_2$ electronic structures. This assumption allowed for bond length changes in the iron-ligand bonds and perturbations of hydrogen-bonding interactions involving the μ-O ligands, which we believe is reasonable at cryogenic temperatures. NRVS spectra for models "cryoreduced" in such a fashion (including spectra for both $^{16}O_2$ and $^{18}O_2$ isotopomers) were calculated and compared to the experimental data in Figure 1A (bottom, black spectrum) and Figure 1B (for the isotope perturbation) as an additional screen for the determination of the geometric and electronic structure of Q.

In the following sections, analyses of the NRVS spectra for OC -OH/=O, OC-OH/-OH, and bis(μO)-L models (where L is H_2O, OH^-, or no water-derived ligand) are presented using the methodology described above.

3.4.1. Open Core Terminal Oxo, Terminal Hydroxide (OC -OH/=O)—

Of the eight OC -OH/=O models, only **OC1**, **OC3**, **OC17**, and **OC26** possess a ν(Fe-OH) + ν_{as}(Fe-O-Fe) mode (ν_2 Figure 4, bottom) near 700 cm^{-1} which would correspond to the resonance Raman feature at 690 cm^{-1}. (Note that the ν_2 modes for OC1 and OC3 exhibit a ^{2}H perturbation of > |8| cm^{-1}, but are included to generally explore the NRVS properties of this structural subclass.) The calculated Q NRVS spectra of these models are provided in Figure 6 (black spectra), and compared to the Early Q – MMOH$_{red}$ data in red (top spectrum; note NRVS calculated spectra for other OC -OH/=O models are provided in Table S1). The experimental data correlate best to the **OC17** NRVS spectrum. Below 300 cm^{-1}, the **OC17** NRVS spectrum exhibits two peaks at 250 and 281 cm^{-1} that dominate the spectrum, and may be correlated to the 275 cm^{-1} and the 300 cm^{-1} peaks in the experimental data. The two peaks in the calculated spectrum at 329 cm^{-1} and 356 cm^{-1} would correlate to the experimental data at 330 and 375 cm^{-1}, respectively, while the calculated less intense 390 and 425 cm^{-1} peaks would correspond to the weak 420 cm^{-1} feature in the data. Hence, below 450 cm^{-1}, the calculated **OC17** NRVS spectrum reasonably correlates to the experimental Q data.

Above 450 cm^{-1}, the calculated **OC17** NRVS spectrum exhibits one peak at 475 cm^{-1}, followed by a lack of intensity up until ~ 700 cm^{-1}, where two peaks are observed at 691 cm^{-1} and 722 cm^{-1}. The experimental data above 620 cm^{-1} show no feature above the increasing high noise within this region (Figure 6, top spectrum, inset on right). However, it is clear that the calculated spectrum does not reproduce the experimental data as there is no calculated peak at 605 cm^{-1}. We thus evaluated whether a vibration of the **OC17** model (and OC -OH/=O models more generally) could reproduce the experimental 605 cm^{-1} peak, with some limited structural perturbation. Vibrations closest to 605 cm^{-1} in the calculated NRVS spectra are color highlighted in Figure 6 and assessed. The calculated vibrations at 691 and 722 cm^{-1} correspond to the ν_3 (ν(Fe-OH) - ν_{as}(Fe-O-Fe); Figure 4 bottom) and ν_2 modes, respectively (red region, Figure 6). The ν_2 mode corresponds to the resonance Raman 690 cm^{-1} feature, and is thus required to be near 700 cm^{-1} based on this assignment. Since ν_3 is the antisymmetric version of ν_2 and is a result of mixing (between the ν(Fe-OH) and ν_{as}(Fe-O-Fe) modes), and since the splitting between ν_2 and ν_3 is ~ 30-40 cm^{-1}, the ν_3 mode cannot be assigned to the 605 cm^{-1} peak without lowering the energy of ν_2 and sacrificing the rR assignment. Note that the 605 cm^{-1} feature cannot be assigned as the isolated ν(Fe-OH) mode in these models, since ν(Fe-OH) + ν_{as}(Fe-O-Fe) mixing is required near 700 cm^{-1} to reproduce the mixed isotope effect in rR of the ν_2 mode. This rules out models such as **OC24** (see NRVS spectrum in Table S1), which possesses a particularly short Fe$_1$=O bond that highly localizes the μ-O ligand on the Fe$_2$ side, resulting in strong μ-O donation to Fe$_2$ and an elongated (1.82 Å) Fe$_2$-OH bond. This model exhibits a localized ν(Fe-OH) vibration near 600 cm^{-1}; however, only the ν_{as}(Fe-O-Fe) mode is observed near 700 cm^{-1}, which would not produce the mixed isotope effect in the rR spectrum (and also would not show resonance enhancement). Thus, neither the ν_2, ν_3, nor an isolated ν(Fe-OH) mode can be assigned to the 605 cm^{-1} peak in the experimental data (indicated by the red X in **OC17** Figure 6).

Vibrations below 600 cm^{-1} were also assessed as possible assignments for the 605 cm^{-1} feature. The region between 440 and 540 cm^{-1} (yellow region Figure 6) includes the ν_s(Fe-O-Fe) mode (ν_4 Figure 4, bottom), as well as terminal carboxylate (ν(Fe-COO$^-$)) stretches that further distribute into the 345 and 440 cm^{-1} region (blue region Figure 6) that mostly contains low energy bending modes (ν_5 and ν_6, see Figure 4 bottom). The energy of the ν_s(Fe-O-Fe) mode (and importantly, the higher energy ν_{as}(Fe-O-Fe) mode) depends primarily on the Fe-O-Fe angle.[59] However, manipulation of the Fe-O-Fe angle to increase the energy of the ν_s(Fe-O-Fe) mode would decrease the energy of the ν_{as}(Fe-O-Fe) mode, which would unacceptably decrease the energy of the ν_2 mode that would be assigned to the 690 cm^{-1} feature in the rR spectrum. Hence, the ν_s(Fe-O-Fe) mode cannot be assigned to the 605 cm^{-1} NRVS feature. The ν(Fe-COO$^-$) modes are too low in energy to be reasonably assigned to the 605 cm^{-1} feature (yellow and blue regions in Figure 6). Their energies are already calculated to be slightly higher than that experimentally observed for a terminal ν(Fe-COO$^-$) mode in a NRVS study[48] of a high-spin Fe(IV) oxo intermediate in SyrB2 at 370 cm^{-1}. Therefore, the 605 cm^{-1} experimental NRVS peak cannot be reasonably correlated to either ν(Fe-COO$^-$) or ν_s(Fe-O-Fe) modes that must be at energies well below 600 cm^{-1}.

In summary, while **OC17** (and OC-OH/=O models in general) reproduces the Q NRVS spectrum reasonably well below 450 cm^{-1}, it fails to capture the 605 cm^{-1} peak in the experimental data. No vibration in the OC-OH/=O models may be reasonably assigned to the 605 cm^{-1} NRVS feature; thus, the OC -OH/=O subclass is excluded as a possible candidate for intermediate Q.

3.4.2. Open Core bis-terminal-hydroxide (OC -OH/-OH)—

The OC -OH/-OH models (14 total) constitute the remaining open core subclass that are to this point in the analysis possible structures of Q. Of these 14 models, 13 possess a symmetric ν(Fe-OH) + ν_{as}(Fe-O-Fe) mode (ν_1 Figure 4) near 690 cm^{-1} with an appropriate $^{16}O^{18}O$ mixed isotope shift, while only 4 of these models (**OC10**, **OC15**, **OC16**, and **OC32**) also exhibit a small ^{2}H isotope effect ($\Delta \leq 3$ cm^{-1}) that would reproduce the rR data. (Models exhibiting a larger ^{2}H isotope effect are **OC9**, **OC11**, **OC13**, **OC18**, **OC19**, **OC20**, **OC23**, **OC33**, **OC34**) The calculated NRVS spectra for **OC10**, **OC15**, **OC16**, and **OC32** are provided in Figure 7A, and NRVS spectra for all remaining OC -OH/-OH models are included in Table S1.

Of the 4 models in Figure 7A, **OC16** best reproduces the experimental data. The calculated NRVS spectrum of **OC16** (Figure 7) below 450 cm^{-1} exhibits an intense feature at 278 cm^{-1}, which may be associated with the 275 cm^{-1} peak in the experimental data (Figure 7A, top red spectrum). The calculated feature at 315 cm^{-1} would correlate reasonably to the 300 peak in the data, while the broad, intense calculated peak at 357 cm^{-1} may be associated with the combination of both the 330 and 375 cm^{-1} features in the data. The 406 cm^{-1} feature may be correlated to the peaks around 420 cm^{-1} in the data; hence, the low energy (< 450 cm^{-1}) region of the calculated **OC16** spectrum reasonably reproduces the Q NRVS spectrum (with similar results for models **OC10**, **OC15**, and **OC32**).

Above 450 cm^{-1}, both **OC16** and **OC32** exhibit intensity near 605 cm^{-1}, whereas **OC10** and **OC15** (as well as the remaining 9 models in the SI) do not. Three vibrations contribute to the calculated **OC16** NRVS spectrum in the region between 600 and 750 cm^{-1}: the rR-assigned ν_1 mode (the symmetric combination of the in-plane ν(Fe$_2$-OH) stretch and ν_{as}(Fe-O-Fe) mode, centered at ~ 712 cm^{-1}); ν_2 (Figure 4 middle), the antisymmetric version of ν_1 (625 cm^{-1}); and ν_3 (Figure 4 middle), the isolated out-of-plane ν(Fe$_1$-OH) mode (666 cm^{-1}). Both the ν_2 and ν_3 modes are possible assignments for the 605 cm^{-1} feature in this structure, with the ν_2 mode closer to 605 cm^{-1}. Interestingly, the ν_1 and ν_2 splitting is larger (40-70 cm^{-1}; red region Figure 7A) in OC -OH/-OH vs. OC -OH/=O models (30-40 cm^{-1}). This is due to the higher symmetry of the OC -OH/-OH models (relative to OC -OH/=O); the two similar Fe-(μ-O) bond lengths result in a lowering of the ν_{as}(Fe-O-Fe) mode to be closer to ν(Fe$_2$-OH) (with a concomitant increase of ν_s(Fe-O-Fe)). This increases the ν_{as}(Fe-O-Fe) + ν(Fe$_2$-OH) mixing, which results in the larger split ν_1 and ν_2 modes. For models **OC10** and **OC15** (and the 9 related models in the SI), the ν_2 mode is at ≥ 650 cm^{-1}, which may not be lowered without sacrificing the rR-assigned ν_1 mode. However, in **OC16**, Glu243 is hydrogen-bonded to Fe$_1$-OH as well as Fe$_2$-OH (see structure in Table S1), which weakens its hydrogen-bonding interactions with Fe$_2$-OH (heavy atom distance increases by 0.1 Å, compared to **OC10**). This decreases the energy of the ν(Fe$_2$-OH) mode, which drives down the energies of both the ν_1 and ν_2 modes. Hence, up until this point in the analysis of this structural class ν_2 is a possible candidate for the 605 cm^{-1} NRVS assignment.

As an additional screen for evaluating **OC16** (and **OC32**; see Figure S27), this model was cryoreduced in DFT to correlate its simulated decay NRVS spectrum to the experimental data in Figure 7B (top, black spectrum). **OC16** was thus optimized with high spin Fe(III)Fe(IV) and Fe(III)$_2$ electronic structures using the methodology outlined above Section 3.4. Optimization of **OC16** to a Fe(III)Fe(IV) species afforded two possible models: Fe$_2$(III)Fe$_1$(IV) or Fe$_2$(IV)Fe$_1$(III), with the Fe$_2$(III)Fe$_1$(IV) model lower in energy by ΔE = −3.4 kcal/mol. The NRVS spectra for the cryoreduced **OC16** Fe$_2$(III)Fe$_1$(IV) and Fe(III)$_2$ models are provided in Figure S26 (middle and bottom rows) in black (structures for the cryoreduced optimized forms are also provided).

To reproduce the decayed Q NRVS decay spectrum in Figure 7B (top in black) which contains a mixture of both Fe(III)Fe(IV) and Fe(III) species, the cryoreduced mixture spectrum (**OC16 Decay**) was prepared by summing 40% of the calculated **OC16** Fe$_2$(III)Fe$_1$(IV) NRVS spectrum and 60% of the Fe(III)$_2$ spectrum from Figure S26A (black spectra). The changes from **OC16** to **OC16 Decay** (Figure 7B middle, red to black) agree with the data (Figure 7B top, red to black), showing shifts of intensity from 288 to 260 cm^{-1} (exp 275 to 220-240 cm^{-1}) and 612 to 590 cm^{-1} (exp 605 to 560-580 cm^{-1}), and decay of the 357 cm^{-1} feature (exp 375 cm^{-1}). The decay of the calculated 612 cm^{-1} and formation of the 590 cm^{-1} features are of particular interest, which in this model would represent the cryoreduced decay of the ν_2 mode corresponding to the 605 cm^{-1} experimental NRVS feature in Q. In the cryoreduced calculation the 590 cm^{-1} feature corresponds to a localized ν(Fe$_2$-OH) mode (Figure 7B, middle); relative to the ν_2 mode in the Fe(IV)$_2$ Q **OC16** model (Figure 7B, middle), this vibration appears downshifted and uncoupled from ν_{as}(Fe-O-Fe) due elongation of the Fe$_2$(III)-OH bond upon cryoreduction. This lowers the energy of the ν(Fe$_2$-OH) mode and limits its mixing with the ν_{as}(Fe-O-Fe) mode. The calculated 590 cm^{-1} feature in **OC16 Decay** also contains contributions from ν_s(Fe-O-Fe) (ν_4 Figure 4), which shifted up in energy (~ 40 cm^{-1}) relative to **OC16** due to a decrease of the Fe-O-Fe angle upon cryoreduction. However, both of these modes would be expected to exhibit signficant $^{18}O_2$ perturbations as both oxygen atoms in the modes must be derived from O_2 based on the rR assignment of the 690 cm^{-1} feature in the $Fe(IV)_2$ structure.

The $^{18}O_2$ spectrum for **OC16 Decay** (**$^{18}O_2$ Q Decay**; Figure 7B bottom, blue spectrum) was prepared by summing 40% of the $^{18}O_2$ **OC16** $Fe_2(III)Fe_1(IV)$ and 60% of the $^{18}O_2$ $Fe(III)_2$ NRVS spectra (provided in Figure S26B, blue spectra). As anticipated, the NRVS spectrum for **$^{18}O_2$ Q Decay** predicts a large (22 cm^{-1}) isotope downshift for the **OC16 Decay** 590 cm^{-1} feature, which does not agree with the 4-7 cm^{-1} shift observed experimentally.

Note that from the analysis above, the ν_4 mode would also exhibit a large isotope dependence in the cryoreduced model (Figure S26B, bottom) and can be excluded. Therefore, the remaining possible assignment for the 605 cm^{-1} feature in the experimental data is the ν_3 mode (ν(Fe_1-OH)) centered at ~ 690 cm^{-1} (note this is slightly upshifted relative to the BP86/10% HF calculation value of 666 cm^{-1}). In the **OC16 Decay** spectrum this mode decreases in energy by 19 cm^{-1}. This mode is not calculated to have an $^{18}O_2$ isotope dependence in the **$^{18}O_2$ OC16 Decay** spectrum (Figure 7B, bottom), since the O_2 loading would occur on the Fe_2-OH and μ-O oxygen atoms. Weak mixing with the ν_4 mode could provide a small ν_3 $^{18}O_2$ isotope shift as observed experimentally. However, the energy of the ν_3 mode at > 650 cm^{-1} (Figure 7A, red column) is too high to reproduce the 605 cm^{-1} NRVS feature and to facilitate mixing with the ν_4 mode. In principle, a model possessing a weaker Fe_1-OH bond and thus a lower energy ν(Fe_1-OH) mode could reproduce the Q 605 cm^{-1} NRVS feature and the 4-7 cm^{-1} isotope shift of the Q decay 580 cm^{-1} feature.

The approximate Fe_1-OH bond length required to produce a 605 cm^{-1} ν(Fe_1-OH) mode was calculated using a Badger's rule analysis (Figure S28).[60] The 605 cm^{-1} feature could be reproduced by a ν(Fe_1-OH) mode corresponding to a 1.85 Å Fe-OH bond length. Models with hydrogen-bond donors to the Fe_1-OH oxygen (**OC9**, **OC13**, **OC21**, **OC33**) result in modest elongation of the Fe-OH bond to 1.76 – 1.78 Å, and exhibit NRVS intensity above 660 cm^{-1} (see Table S1). Indeed, none of the 14 OC -OH/-OH models reproduce this long Fe_1-OH bond corresponding to a ν(Fe_1-OH) mode near 605 cm^{-1}.

To summarize, the OC -OH/-OH subclass reasonably reproduces the low-energy (< 450 cm^{-1}) region of the Q NRVS spectrum. However, the $^{18}O_2$ 4-7 cm^{-1} isotope shift of the 560-580 cm^{-1} feature in the Q decay data eliminates assignment of the Q 605 cm^{-1} NRVS feature to vibrations strictly containing motion of the in-plane Fe_2-OH and μ-O ligands. The one plausible assignment of the 605 cm^{-1} feature in the OC -OH/-OH structure is the out-of-plane ν_3 (ν(Fe_1-OH)) mode; however, the calculated Fe_1-OH bond length is too short in the OC -OH/-OH subclass (due to the relatively low donor strength of the ligands on Fe_1) to produce a ν_3 mode near this energy. The relatively high energy of this mode prevents mixing with the ν_4 mode that would be required for the $^{18}O_2$ 4-7 cm^{-1} isotope shift of the Q decay 580 cm^{-1} feature. Though the assignment of Q to the OC -OH/-OH subclass is not well-supported by our calculations, we leave it as an open possibility pending further experimental evidence.

3.4.3. Closed core—

The closed core subclasses available as possible assignments for Q are the bis(μO), bis(μO)-H_2O, and bis(μO)-OH models. The subset of these models possessing an appropriate $^{16}O^{18}O$ mixed isotope shift include all 6 bis(μO) models (**bis(μO)-1-6**), 12 out of 16 of bis(μO)-H_2O models (**bis(μO)-H_2O-1-4, 6, 8-12, 14-15**), as well as 9 out of 16 of the bis(μO)-OH models (**bis(μO)-OH-6, 8, 10-16**). The NRVS spectra for all closed core models are included in Table S1 (along with their structures).

Of these remaining models, four models (**bis(μO)-OH-6, bis(μO)-OH-8, bis(μO)-OH-10, bis(μO)-H_2O-14**) lack in their calculated NRVS spectra the characteristic 275 cm^{-1} signal present in the early Q data (Figure 8A, red spectrum) and are therefore excluded from further analysis. The calculated NRVS spectrum of **bis(μO)-H_2O-6** corresponds particularly well to the early Q NRVS data, and is representative of the NRVS spectral behavior of the possible bis(μO) and bis(μO)-H_2O closed core models. Below 450 cm^{-1}, the **bis(μO)-H_2O-6** NRVS spectrum (Figure 8B) exhibits one intense feature at 267 cm^{-1}, which may be associated with the intense 275 cm^{-1} peak in the early Q data (Figure 8A, red spectrum). At higher energy, four peaks of moderate intensity are calculated at 306, 349, 378 and 413 cm^{-1}, which would correspond to the features in the experimental data at 300, 330, 375, and 420 cm^{-1}. Thus, below 450 cm^{-1}, the calculated NRVS spectrum for **bis(μO)-H_2O-6** reproduces the early Q NRVS data reasonably well.

Above 450 cm^{-1}, two features of similar intensity are calculated at 614 and 631 cm^{-1}. These two features correlate well to the early Q NRVS feature at 605 cm^{-1}; indeed, all 23 possible closed core models possess features between 600 and 640 cm^{-1} which could correspond to the 605 cm^{-1} feature in the early Q NRVS data. In **bis(μO)-H_2O-6**, the two features calculated at 614 and 631 cm^{-1} correspond to the B_{2u} (ν_3 Figure 4) and B_{3u} (ν_2 Figure 4) non-symmetric modes of the Fe_2O_2 core. The remaining high-energy Fe_2O_2 stretching mode, the A_g breathing mode of the core (ν_1 Figure 4) that would be assigned to the 690 cm^{-1} rR vibration, is calculated at 693 cm^{-1} and is much weaker in NRVS than the non-symmetric modes. Therefore, at this point in the analysis, the high-energy (> 450 cm^{-1}) region of the early Q NRVS data may reasonably be assigned to the non-symmetric Fe_2O_2 stretches of **bis(μO)-H_2O-6** (as well as in the other closed core models).

The **bis(μO)-H_2O-6** and related acceptable models were then further screened through NRVS calculations based on their cryoreducted DFT structures for correlation to the decayed Q data (Figure 8A, black spectrum). For the H_2O-Fe_2-(μ-O)$_2$-Fe_1 structure of **bis(μO)-H_2O-6**, optimization to an Fe_2(III)Fe_1(IV) electronic structure was lower in energy by 2.8 kcal/mol. The decay spectrum for **bis(μO)-H_2O-6** (**bis(μO)-H_2O-6 Decay**) is shown in Figure 8C (40% Fe_2(III)Fe_1(IV) and 60% Fe(III)$_2$, their individual NRVS spectra are shown in Figure S29A (ii) and (iii)). The spectral differences between **bis(μO)-H_2O-6** and **bis(μO)-H_2O-6** Decay (Figure 8C red to black) correlate well to the decay of Q features in the beam (Figure 8A, red to black), which include decay of the intense 267 cm^{-1} feature (exp 275 cm^{-1}) with growth of features between 190 and 215 cm^{-1} (exp 220-240 cm^{-1}), decay of the 378 cm^{-1} feature (exp 375 cm^{-1}), and a downshift in energy of the 631 cm^{-1}

feature (exp 605 cm^{-1}) to 560 cm^{-1} (exp 560 to 580 cm^{-1}). Though the downshift of the calculated 631 cm^{-1} feature agrees with experiment, this mode corresponds to the ν_2 non-symmetric stretch of the Fe_2O_2 core and is calculated to have an $^{18}O_2$ isotopic shift (> 20 cm^{-1}; Figure 8D) larger than accommodated by the experimental data (4-7 cm^{-1} from Figure 1B). However, the related closed core models with the axial H_2O replace by an OH^- are consistent with experiment.

Unlike the bis(μO) and bis(μO)-H_2O subclasses, the bis(μO)-OH models possess an additional mode between 600-700 cm^{-1} corresponding to the ν(Fe-OH) stretching mode, and are therefore further evaluated. The calculated NRVS spectrum for **bis(μO)-OH-12** is given in Figure 9B (and its structure is given in Figure 10). Below 500 cm^{-1}, the calculated NRVS spectrum correlates well to the experimental data (Figure 9A, red spectrum), exhibiting one intense peak at 270 cm^{-1} (exp 275 cm^{-1}), three additional features at 300 cm^{-1} (exp 300 cm^{-1}), 336 cm^{-1} (exp 330 cm^{-1}) and 381 cm^{-1} (exp 375 cm^{-1}), and intensity at 428 and 467 cm^{-1} (exp 420 cm^{-1}). Above 450 cm^{-1}, the calculated spectrum shows a shoulder at 589 cm^{-1}, followed by strong intensity between 604 - 621 cm^{-1} (with a shoulder at ~ 620 cm^{-1} and a weak feature at 692 cm^{-1}. The intense peak at ~ 604 cm^{-1} corresponds to the ν(Fe-OH) mode, while the remaining intensity corresponds to the breathing mode (692 cm^{-1}; assigned to the rR feature at 690 cm^{-1}) and two of the non-symmetric core modes (589 and ~ 620 cm^{-1}). Interestingly, this ν(Fe-OH) mode is downshifted by more than 50 cm^{-1} compared to the out-of-plane ν(Fe-OH) mode in the OC - OH/-OH subclass (Section 3.4.2). This reflects the longer Fe-OH bond length in the bis(μO)-OH (~ 1.83 A) vs. OC -OH/-OH (~ 1.77 A) models, due to the bis(μO) bridges providing a stronger donating equatorial core. From correlation to the experimental Q NRVS data, any one of the calculated three modes in the **bis(μO)-OH-12** NRVS spectrum between 580 cm^{-1} and 630 cm^{-1} could correspond to the Q NRVS feature at 605 cm^{-1}.

The **bis(μO)-OH-12** model was further evaluated by DFT calculated cryoreduction to Fe(III)Fe(IV) and $Fe(III)_2$ electronic structures. Optimization on the Fe(III)Fe(IV) level yielded both Fe_2(III)Fe_1(IV) and Fe_2(IV)Fe_1(III) models (hydroxide bonded to Fe_2) differing in energy by only 1.5 kcal/mol. Therefore, the NRVS spectra of both models are included in the analysis of the cryoreduction data. Additionally, optimization of **bis(μO)-OH-12** to an $Fe(III)_2$ structure resulted in proton transfer from Glu144 to the μ-O bridge it hydrogen-bonds to in the Q structure (Figure 10); structures and bond lengths of these cryoreduced models are found in Figure S30 and Table S13, respectively.

The cryoreduced NRVS spectrum of **bis(μO)-OH-12** (**bis(μO)-OH-12 Decay**) was generated by combining 20%, 20%, and 60% of the **bis(μO)-OH-12** Fe^2(III)Fe_1(IV), Fe_2(IV)Fe_1(III), and $Fe(III)_2$ NRVS spectra (Figure S30 (ii), (iii), and (iv)). The spectral changes from **bis(μO)-OH-12** to **bis(μO)-OH-12 Decay** (Figure 9C, red to black) correlate reasonably well to the changes in the Q NRVS spectrum observed in the beam (Figure 9A, red to black). Decay of the calculated feature at 270 cm^{-1} (exp 275 cm^{-1}) is observed with concomitant growth of intensity between 180-215 cm^{-1} (exp 220-240 cm^{-1}), as well as decay of a feature at 381 cm^{-1} (exp 375 cm^{-1}). At high energy, a downshift of calculated intensity is observed in the 604-621 cm^{-1} region (exp 605 cm^{-1}) to 560-583 cm^{-1} (exp 560-580 cm^{-1}), corresponding to a decrease in the energies of the non-symmetric stretches and ν(Fe-OH) mode. Note that, in the distorted Fe(III)Fe(IV) and (μ-OH)(μ-O) Fe(III)$_2$ structures of the cryoreduced models, the Fe-O core stretches localize (therefore, Fe-(μ-O) stretching modes are indicated as ν(Fe-O) in black in Figure 9C).

The calculated $^{18}O_2$ NRVS spectrum of **bis(μO)-OH-12 Decay** (**$^{18}O_2$ bis(μO)-OH-12 Decay**) reveals a striking difference in the isotope sensitivity of the high energy region ~ 600 cm^{-1}) relative to the other bis(μO) subclasses (Figure 9D black to blue). Vibrational modes with Fe-(μ-O) stretching motion above 500 cm^{-1} exhibit $^{18}O_2$ downshifts larger than 20 cm^{-1}, which are not observed in the experimental data (Δ = 4-7 cm^{-1}) and is similar to the findings for the bis(μO) and bis(μO)-H$_2$O subclasses. However, a significant peak at 583 cm^{-1} in the **bis(μO)-OH-12 Decay** NRVS spectrum does not exhibit an isotope shift in the calculated $^{18}O_2$ spectrum (Figure 9D). This corresponds to the ν(Fe$_2$-OH) mode, for which the hydroxide oxygen atom remains unlabeled upon $^{18}O_2$ loading. Note that the limited 4-7 cm^{-1} isotope shift observed would reflect some mixing with the non-symmetric Fe$_2$O$_2$ core modes in this energy region (as observed in the calculated **bis(μO)-OH-16** NRVS spectra: see Figure S31). Indeed, in comparison to all other subclasses of models analyzed, the bis(μO)-OH subclass best reproduces the two defining characteristics of the Q 605 cm^{-1} NRVS feature: the small $^{16}O_2 \rightarrow {}^{18}O_2$ 4-7 cm^{-1} isotope shift in the Q decay NRVS spectrum, which reflects the unlabeled Fe-OH bond; and the low energy of this ν(Fe-OH) stretch, reflecting the increased Fe$_2$-OH bond length due to the strong equatorial (μ-O)$_2$ donation in the bis(μO)-OH core. *Hence, of the 90 models evaluated in this study, the closed core bis(μO)-OH subclass* (Figure 10) *best reproduces the Q and Q decay NRVS data in the higher energy region*.

With the assignment of this subclass as the best candidate for the structure of Q, assignment of the Q and Q decay NRVS spectra is now provided (Figure 9B) using **bis(μO)-OH-12**. The most intense mode (Figure 9B) calculated at 270 cm^{-1} (exp 275 cm^{-1}) corresponds to two ν(Fe-N) stretching modes. The decay of these features with concomitant growth of intensity between 180 - 215 cm^{-1} (exp 220-240 cm^{-1}) in **bis(μO)-OH-12** decay reflects elongation of the Fe-N bonds upon cryoeduction. The two features at 300 cm^{-1} (exp 300 cm^{-1}) and 336 cm^{-1} (exp 330 cm^{-1}) are assigned to the A_g accordion (ν_5 Figure 4) and A_u butterfly (ν_6 Figure 4) modes of the closed core, respectively. These vibrations primarily reflect bending motions of the Fe$_2$O$_2$ core, with force constants less dependent on Fe-ligand bond lengths; thus, upon cryoreduction, the energy of these vibrations remains relatively unchanged. The feature at 381 cm^{-1} (exp 375 cm^{-1}) is assigned to a ν(Fe-COO$^-$) terminal carboxylate stretch, and decay of this feature reflects an elongation of the Fe-COO$^-$ bond upon cryoreduction. The two calculated peaks between 428 and 467 cm^{-1} (exp 420 cm^{-1}) correspond to the Fe$_2$O$_2$ core B_{1g} mode (ν_4 Figure 4), mixed into symmetric and antisymmetric combinations with a nearby terminal carboxylate stretching mode. In the cryoreduced models, the structure distorts and the core modes localize (indicated in Figure 9C by ν(Fe-O) in black). The cryoreduced Fe(III)$_2$ (μ-O)(μ-OH) model now has μ-OH antisymmetric ν_{as}(Fe-OH-Fe) and symmetric ν_s(Fe-OH-Fe) modes. The lowest energy ν(Fe-O) and ν_s(Fe-OH-Fe) modes are calculated to be between 400 and 450 cm^{-1}, in a similar energy regime as the B_{1g} mode in **bis(μO)-OH-12**, and exhibit an $^{18}O_2$ downshift in **$^{18}O_2$ bis(μO)-OH-12 Decay** (16 cm^{-1}) that corresponds well to the isotope shift of the 420

cm^{-1} NRVS feature in Q decay (12-15 cm^{-1}). Finally, as presented above, non-symmetric Fe_2O_2 core stretches as well as the $\nu(Fe_2\text{-}OH)$ mode are calculated to be between 589 – 621 cm^{-1} in the Q model, which lower in energy to 560-583 cm^{-1} in **bis(μO)-OH-12 Decay**. However, from the data the $\nu(Fe_2\text{-}OH)$ mode (calc ~ 604 cm^{-1}) is mostly observed in the NRVS spectrum, based on the limited $^{16}O_2$ and $^{18}O_2$ sensitivity of the 560 – 580 cm^{-1} region in the Q decay data.

In the process of completing this study, a higher resolution XFEL structure was published (Srinivas et al., 2020)[56] of MMOB-associated MMOH. Compared to the crystal structure (PDB: 4GAM) of the MMOB/MMOH complex used for the analysis herein,[54] the XFEL-derived structure exhibits two oxygenic bridging ligands as well as monodentate ligation of Glu114, Glu243, and Glu209 (in contrast to their bidentate ligation in 4GAM, likely due to cryoreduction).[56] Small differences in the C_α constraints are also observed in Glu114 (Δ = 0.80 Å) and Glu243 (Δ = 0.46 Å). The influence of these structural changes on our computational models was determined by generating **bis(μO)-H$_2$O-1** and subsequent models of Q from the XFEL-derived structure and resimulating their NRVS spectra (Figure S32). These XFEL-derived structures are very similar and their calculated NRVS spectra show negligible deviations from those used in this analysis.

3.5. Correlation to Reactivity

Intermediate Q in sMMO (*Mt* OB3b) abstracts an H atom from methane with a kinetic barrier $\Delta G^\ddagger$ of 10.3 kcal/mol.[31,61] For comparison, the mononuclear non-heme iron enzyme Fe(IV)=O intermediate in SyrB2 has a $\Delta G^\ddagger$ ~ 17.7 kcal/mol for H-atom transfer (HAT) from threonine at the same temperature.[62] This can be propagated to the stronger C-H bond of CH_4 (cf. ΔH_{BDE}(threonine) ~ 94 kcal/mol vs. $\Delta H_{BDE}(CH_4)$ ~ 104.5 kcal/mol). This 10 kcal/mol worse thermodynamics would raise the HAT reaction barrier between the Fe(IV)=O site in SyrB2 and CH_4 to ~ 24 kcal/mol. Thus, the binuclear Fe(IV) intermediate Q is far more reactive than the mononuclear NH Fe(IV)=O intermediate. This substrate-adjusted kinetic barrier for SyrB2 is well reproduced by reaction coordinate calculations, which predict $\Delta G^\ddagger$ ~ 22.1 kcal/mol for the CH_4 reaction in Figure 11(a) and Table 1.

Three binuclear models, **OC26** (-OH/=O), **OC15** (-OH/-OH), and **bis(μO)-OH12**, have been evaluated for their H-atom abstraction ability relative to this mononuclear site. The Fe(IV)=O site of the OC -OH/=O model is predicted to react with CH_4 at a similar rate as SyrB2, with the calculated $\Delta G^\ddagger$ ~ 25.0 kcal/mol. While this reaction appears more driven by the thermodynamics (ΔΔE ~ 6 kcal/mol and ΔΔG ~ 4 kcal/mol), this difference is due to an H bond that forms to the OH group of OC26 generated upon H-atom abstraction (HAA). Without this H-bond, the HAA product of the OC -OH/=O model is destabilized by 5 and 8 kcal/mol in potential energy and free energy, respectively (Figure S33). These energy profiles indicate that the activity of the Fe(IV)=O site is similar, regardless of whether it is present in a mononuclear or OC μ-O bridged binuclear site.

The H atom abstraction from CH_4 by the Fe(IV)-OH site in the open-core -OH/-OH model has a kinetic barrier of $\Delta G^\ddagger$ ~ 15.4 kcal/mol and the calculated thermodynamics of ΔG ~ −2.1 kcal/mol. These values are 9.6 and 12.5 kcal/mol lower than those of the Fe(IV)=O site in the OC -OH/=O model, respectively, showing that the Fe(IV)-OH system can be more reactive than the Fe(IV)=O system. When Marcus theory is used to remove the thermodynamic contribution to the barrier, the intrinsic barriers obtained for the Fe(IV)=O and Fe(IV)-OH systems are similar (last column in Table 1; Figure S34). Thus, the lower HAA barrier of the Fe(IV)-OH system is attributed to its greater thermodynamic driving force relative to the Fe(IV)=O system. Indeed, a hypothetical mononuclear Fe(IV)-OH site in SyrB2 was evaluated and gave similar thermodynamics to the -OH/-OH model (Figure S34). Upon HAA, the Mayer bond order between the Fe and the O decreases by 0.883 for the Fe(IV)=O to Fe(III)-OH conversion while it is 0.718 for the Fe(IV)-OH to Fe(III)-OH_2 conversion, implying that the latter costs less energy and is thus more favorable. The calculated barrier for the open-core -OH/-OH model of $\Delta G^{\ddagger}$ ~ 15.4 kcal/mol is comparable to the experimental barrier ($\Delta G^{\ddagger}$ ~ 10.3 kcal/mol) measured for intermediate Q. Interestingly, the strong HAA reactivity of the M(IV)-OH unit (M = metal) agrees with findings from a recent study on corrole model complexes, in which the Mn(IV)-OH complex was found to be more reactive than the Mn(V)=O analog.[63]

The preferred closed core model based on the NRVS data contains the bis(μO) bridges and the terminal OH ligand, which differs from previously suggested models that instead contain a terminal water ligand or two μ-1,3-carboxylato bridges with no water-derived ligands.[64-68] This closed core model is calculated to be much more reactive than the mononuclear Fe(IV)=O and OC -OH/=O models, with $\Delta G^{\ddagger}$ ~ 12.4 kcal/mol and ΔG ~ −1.0 kcal/mol (Table 1). This low barrier agrees well with the experimental barrier of intermediate Q. The origin of this high HAA activity of the closed-core relative to the open-core systems reflects their key structural difference. As presented above, the open-core models are very similar to the corresponding mononuclear systems in terms of HAA activity. In contrast, the 2nd μ–O bridge of the closed core systems cooperates with the H atom-accepting μ–O bridge, signifying a key role of the 2nd Fe center in the HAA process. More details will be discussed below.

4. Discussion

In this study, we have systematically evaluated a significant range of open and closed core candidate structures of intermediate Q and assessed their viability in reproducing prior experimental as well as newly acquired NRVS data. Though the original 2.46 Å Fe-Fe distance favoring a closed core structure for Q has been determined to be an artifact,[43] still reasonable evidence for this assignment was provided by resonance Raman spectroscopy[28] that showed the presence of a 690 cm^{-1} vibration exhibiting an averaged $^{16}O^{18}O$ mixed isotope shift. Herein, our analysis of closed core models of Q has shown that a subset of these models also possessing carboxylate (bis(μO)), water (bis(μO)-H_2O), and hydroxide (bis(μO)-OH) axial ligands would show a resonance-enhanced Raman vibration near 690 cm^{-1} with the appropriate isotope perturbations. From TD-DFT calculations of absorption spectra, the transitions associated with the 351 nm line excitation for the closed core structure correspond to charge transfers from both μ-O bridges to both Fe(IV) ions. Such an excited state would result in elongations of all four Fe-(μ-O) bonds, leading to resonance enhancement of the A_g breathing mode characteristic of $M_2(\mu\text{-}O)_2$ (M = metal) cores[29,30,69] (ν_1 at 690 cm^{-1} in $Fe(IV)_2(\mu\text{-}O)_2$, Figure 4, top). Incorporation of $^{16}O^{18}O$ into the $(\mu\text{-}O)_2$ core would provide the observed mixed isotope shift.

However, the analysis presented here shows that the experimental 690 cm^{-1} rR feature and its $^{16}O^{18}O$ shift are not necessarily indicative of a closed core geometry. Two subclasses of open core models have been identified that are predicted to reproduce the rR data for Q: HO-Fe_2(IV)-O-Fe_1(IV)=O (OC -OH/=O) and HO-Fe_2(IV)-O-Fe_1(IV)-OH (OC -OH/-OH; Fe_1-OH vector oriented out of the Fe-O-Fe plane). Interestingly, the calculated TD-DFT absorption spectra for both subclasses (as well as the closed core subclasses) are similar, predicting a low-energy region (8,000 – 15,000 cm^{-1}) comprised of Fe(IV) *d-d* transitions, followed by a region (15,000 – 23,000 cm^{-1}) of μ-O and OH^- LMCTs to the exchange-stabilized *dx^2-y^2 LUMO*. Above 23,000 cm^{-1} (and relevant to the 351 nm/28,500 cm^{-1} rR excitation) TD-DFT calculations predict μ-O and OH^- charge transfer to *localized dπ** orbitals of the $Fe(IV)_2$ centers. Such an excited state would result in a symmetric elongation of the in-plane Fe_2-OH and Fe_2-(μ-O) bonds. In the OC -OH/=O and -OH/-OH subclasses, this excited state distortion would result in the resonance enhancement of the ν(Fe_2-OH) + ν_{as}(Fe-O-Fe) symmetric stretching mode (ν_2 Figure 4 bottom, and ν_1 Figure 4 middle, respectively) near 700 cm^{-1} that would reproduce the 690 cm^{-1} experimental feature. Hence, the resonance Raman data for Q do not rule out an open core structural assignment.

Unlike resonance Raman, NRVS observes all vibrations of a ^{57}Fe active site with iron motion and has been used in this study to probe the vibrational spectrum of intermediate Q up to 720 cm^{-1}. The NRVS data of Q (Figure S3) exhibit time-dependent changes in the beam, most dramatically the rapid decay of an intense feature at 275 cm^{-1} in the early time data with concomitant growth of intensity between 220-240 cm^{-1} in later scans. Tracking this feature during the NRVS measurement allowed for quantitative chronological binning of the data and elucidation of intermediate Q vs. Q decay NRVS features (Figure 1A), which allowed identification of a key additional feature at 605 cm^{-1} associated with the Q NRVS spectrum that downshifted to 560 - 580 cm^{-1} in Q decay. The DFT simulations of the NRVS spectra for the Q models predict an intense low energy (< 300 cm^{-1}) feature for both open and closed core structural subtypes due to Fe(IV)-N(His) vibrations; hence, the 275 cm^{-1} NRVS feature is a distinguishing feature of Q but is not characteristic of a particular structure. In contrast, these simulations have shown that the energy of the 605 cm^{-1} NRVS feature, as well as the $^{16}O_2 \rightarrow {}^{18}O_2$ 4 – 7 cm^{-1} isotope shift of the 560 - 580 cm^{-1} NRVS feature of Q decay (Figure 1B), does enable evaluation of possible structural subtypes for intermediate Q.

Indeed, the presence of this high-energy NRVS feature eliminates the assignment of an OC -OH/=O structure to Q. This subclass had been postulated as a structural candidate for Q based on the high C-H bond reactivity of an OC -OH/=O model complex relative to its closed core precursor,[40] as well as the intense pre-edge region of Q that derives from 3d-4p mixing requiring a non-centrosymmetric environment, thought to reflect the terminal Fe(IV)=O unit in a μ-O bridged open core.[42] However, the OC -OH/=O model calculations cannot reproduce both the experimental 605 cm^{-1} NRVS and 690 cm^{-1} rR features. A strong Fe_1=O oxo bond would result in a long Fe_1-(μ-O) and short Fe_2-(μ-O) bond, resulting in a long Fe_2-OH bond that would exhibit a stretching mode near 605 cm^{-1} (Figure 12); however, this would result in an isolated ν_{as}(Fe-O-Fe) mode above 700 cm^{-1} that would not reproduce the resonance-enhanced mixed isotope shift of the 690 cm^{-1} rR feature. A weak Fe_1=O oxo bond (facilitated through hydrogen-bonding interactions) would reverse this effect, raising the energy of the ν(Fe$_2$-OH) mode to near 690 cm^{-1} that allows its mixing with ν$_{as}$(Fe-O-Fe) thus reproducing the rR feature and its isotope shifts. However, in this case, no mode near 605 cm^{-1} would be observed that could be assigned to the NRVS feature in Q. Therefore, due to the donor strength of the terminal oxo and its distortion of the OC -OH/=O core, this subclass cannot accommodate both a 605 cm^{-1} NRVS and a 690 cm^{-1} rR feature. A strong oxo can distort the core to provide the NRVS feature, and a weak oxo can distort the core to reproduce the rR feature – but the presence of the oxo prevents both.

The possibility of a new open core structural type, OC -OH/-OH, was further raised in this study and evaluated against the Q and Q decay NRVS data. With two Fe-OH bonds, this model could in principle account for both the 605 cm^{-1} NRVS feature and the small isotope shift of the Q decay 560 - 580 cm^{-1} feature (via the out-of-plane Fe$_1$-OH, which has not incorporated O$_2$ but could mix weakly with the μ-^{18}O bridge), and the 690 cm^{-1} resonance Raman feature and its mixed isotope shifts (due to mixing of the O$_2$-labeled in-plane Fe$_2$-OH and μ-O modes). However, all OC -OH/-OH models evaluated in this study possess ν(Fe$_1$-OH) modes above 650 cm^{-1} reflecting their relatively short Fe$_1$-OH bonds (1.76 Å). Hydrogen bonding to the Fe$_1$-OH oxygen resulted in a modest elongation of the bond, but did not result in a calculated ν(Fe$_1$-OH) mode near 605 cm^{-1} that would require a ~ 1.85 Å Fe$_1$-OH bond length. However, even if a long Fe$_1$-OH bond was obtained, this would shorten the Fe$_1$-(μ-O) bond and elongate the Fe$_2$-(μ-O) bond, thus strengthening the Fe$_2$-OH bond (Figure 12). A structure with short Fe$_2$-OH and long Fe$_2$-(μ-O) bonds would likely eliminate the ν(Fe$_2$-OH) + ν$_{as}$(Fe-O-Fe) coupling required to reproduce the mixed isotope shift of the rR 690 cm^{-1} feature. While our study has not identified a viable OC -OH/-OH model that satisfies the isotope sensitivity of the Q 690 and Q decay 560 - 580 cm^{-1} features, we leave this model as a possible assignment for Q contingent on further experimental data.

Analysis of the predicted NRVS spectra for closed core models has yielded an assignment for Q that satisfies both the rR and NRVS data. Of all 90 DFT models considered in this report, the bis(μO)-OH subclass best reproduces the low energy of the 605 cm^{-1} feature in the Q NRVS spectrum and the 4-7 cm^{-1} ^{18}O$_2$ isotope shift in the cryoreduced data (between 560 - 580 cm^{-1}) *and is our favored assignment for Q*. The closed core bis(μO)-OH subclass possesses an additional mode near 605 cm^{-1} that corresponds to the ν(Fe$_2$-OH) stretching mode. The low energy of this mode reflects the strongly donating (μ-O)$_2$ equatorial ligand field, which results in an elongated Fe$_2$-OH bond (~ 1.83 Å) compared to the OC -OH/-OH models (Figure 12). The ν(Fe$_2$-OH) mode would show only limited ^{18}O$_2$ isotope dependence in the Q decay NRVS spectrum, since O$_2$ would be loaded into the (μ-O)$_2$ core and thus the isotope shift of this mode would be contingent on mixing with non-symmetric core modes. It should be qualified that this assignment of Q using NRVS assumes the DFT-calculated cryoreduced structures are reasonable allowing use of the isotope perturbations. However, in the DFT analysis of the cryoreduced data the NRVS spectra clearly exclude the OC -OH/=O subclass.

This assignment of Q is also consistent with past spectroscopic results. From Mössbauer spectroscopy, the two iron ions are fairly equivalent but show a measurable difference in the *Mc* Bath variant. Mössbauer calculations herein (Table S14) on a variety of models demonstrate that the isomer shifts are fairly similar for all subclasses, while the quadrupole splitting shows some variability in the difference (ΔE_{Q1}-ΔE_{Q2}). In the bis(μO)-OH subclass, this difference in quadrupole splitting between the two iron ions is found to primarily depend on the axial carboxylate Glu144-Fe_2 interaction (Figure 10), in which a stronger interaction leads to a smaller ΔE_{Q1}-ΔE_{Q2}. From TD-DFT XAS calculations in the SI (Figure S35), the bis(μO)-OH subclass would be consistent with the increased pre-edge intensity of Q as long as at least one Fe(IV) is 5C. Additionally, while an active site with two 6C Fe(IV) would have a K-pre-edge spectrum with a well split $d\pi$-$d\sigma$ pattern with only the $d\sigma$ being intense, the presence of at least one 5C Fe(IV) site reduces the energy of its dz^2 peak and produces additional dipole character in the $d\pi$ peak, consistent with the experimental spectrum (Figure S35). The Fe-Fe distance of 3.4 Å from HERFD-EXAFS[43] is more of an issue. However, the published data contain 50-60% biferrous with a distance of 3.27 Å, and had been extrapolated from a narrow k range of 2 to 11 $Å^{-1}$ which affects[70] the Fourier transform that had been fit in the analysis. These fits show two Fe-Fe contributions at 3.05 and 3.30 Å. While the longer distance would rule out a closed core species, elongation of the Fe-Fe distance to 3.0 Å in bis(μO)-OH models costs 2-5 kcal/mol and shifts the resonance Raman active A_g breathing mode down by at least 40 cm^{-1} (with the correct isotope shifts; see Table S15). The NRVS spectra of these closed core Fe-Fe elongated models exhibit only modest changes near 600 cm^{-1}, due to elongation of the Fe-μ-O bonds that shifts core modes to lower energy while shortening the ν(Fe_2-OH) bond and increasing its vibrational energy by ~ 10 cm^{-1} (Figure S36).

The DFT-calculated HAA activity of the closed-core bis(μO)-OH models reproduces the experimental value for intermediate Q. Compared to the mononuclear non-heme Fe(IV)=O site in SyrB2, this closed core model has a lower kinetic barrier by ~10 kcal/mol for HAA from CH_4 (Table 1). Given the similarity in intrinsic barriers, the lower barrier of the closed core model can be attributed to the greater thermodynamic driving force for HAA relative to the mononuclear Fe(IV)=O system ($\Delta\Delta G \sim -15$ kcal/mol). Figure 13 illustrates the origin of this favorable thermodynamics of the binuclear closed-core system based on the concerted motion of the bis(μO) bridges. For the case of the mononuclear system, upon HAA, only the Fe(IV)=O bond significantly changes, while the other ligand-Fe bonds only show minor changes (Figure S37). Alternatively, for the closed-core models, all four Fe(IV)-μO bonds undergo significant variations upon HAA; while Fe_2 and μO_a in Figure 13 accept the electron and proton of the H atom, respectively, the Fe_2-μO_b bond is comparably weakened with a MBO decrease of 0.381. Notably, the weakening of the Fe_2-μO_b bond is compensated by forming a stronger μO_b bond to the Fe_1 center with an increase in MBO of 0.463 (Figure S38). If the Fe_1-μO bonds are kept frozen during HAA, the reaction thermodynamics is predicted to become more endergonic by 12 kcal/mol (Figure 13(b), bottom), equivalent to that of the mononuclear system. Thus, the concerted motion of the bis(μO) bridges coupled to the second Fe center drives the HAA process. After HAA, the rebound of the $CH_3\cdot$ radical can occur with a barrier of $\Delta G^{\ddagger} \sim 8.4$ kcal/mol, lower than the HAA barrier of $\Delta G\ddagger \sim 12.4$ kcal/mol, via opening of the core with the dissociation of the Fe_2(III)-μO_a bond (Figure S39).

For the case of the OC -OH/-OH model, this compensation effect from the second Fe center is not significant, as the OC -OH/-OH model is calculated to show similar thermodynamics to that of a hypothetical mononuclear Fe(IV)-OH system (Figure S34). Based on its similar calculated low-energy $\Delta G^{\ddagger}$ (15.4 vs. 12.4 kcal/mol for the closed core), the -OH/-OH model could also be a candidate for HAT from CH_4. Importantly, the reactivity of the two terminal OH ligands would be constrained by the O_2 labeling results. From the rR data, one oxygen atom from O_2 remains in the μO bridge after HAT, while the other oxygen atom from O_2 is incorporated into the CH_3OH product.[32] Since the HAT and the hydroxyl rebound cannot occur from the same OH group, the OH group that abstracts the H atom from CH_4 must be water-derived. However, unlike the bridging oxygen, the terminal OH ligands can undergo isotope scrambling, which was not observed in the rR data.[28] Further, this HAT-active OH group would also have to be out of the Fe-μO-Fe plane, because the in-plane OH group must be derived from O_2 to reproduce the $^{16}O^{18}O$ mixed isotope effect for the rR feature[28] at 690 cm^{-1}. Therefore, to match existing data, the out-of-plane OH group of the -OH/-OH model would have to abstract the H atom, while the in-plane OH group would need to react with the CH_3 radical to form CH_3OH. However, if CH4 can access the in-plane OH group, it is also able to perform HAT with an even lower barrier of $\Delta G^{\ddagger}$ ~ 10.2 kcal/mol (Figure S40). Thus, while the binuclear nature of the site might enable the formation of the Fe(IV)-OH group in the -OH/-OH model, which is capable of HAT and rebound to form CH_3OH with a low barrier (Figure S41), there would have to be limited terminal OH^- ligand exchange and major positional control of non-polar molecules (CH_4 and $CH_3\cdot$) by the active-site pocket.

While finalizing this manuscript, another study was published which computationally evaluates previous data on intermediate Q.[71] This study raised the idea that the resonance Raman data of Q can be consistent with an open core structure, which is consistent with our results. However, the authors of this work favor an OC -OH/=O active site geometry, inconsistent with our NRVS data and in particular the 605 cm^{-1} NRVS feature that excludes this assignment of Q. Additionally, we calculate that this open core structural subclass possesses similar reactivity towards methane as a mononuclear Fe(IV)=O system, inconsistent with the higher reactivity of Q relative to mononuclear non-heme iron enzymes. Alternatively, we do find that closed core models predict larger reactivity due to the compensating effect of the spectator μ-oxo bridge, and additionally find that the OC -OH/-OH subclass may also reproduce the high reactivity of intermediate Q.

5. Conclusion

In this study, NRVS has been used to probe all vibrational modes of intermediate Q and its decay product having Fe motion, thus providing important complimentary information to findings from other spectroscopic techniques. Analyzing these data with DFT calculations provides an experimentally supported geometric/electronic structure for Q that has been combined with kinetic data to obtain insight into its unique reactivity. The analysis herein supports a closed bis(μO) $Fe(IV)_2$ core for Q, where its high reactivity reflects the compensating effect of the μ–O bridge *not* involved in the H-atom abstraction. This application of NRVS to intermediate Q highlights the power of this technique in characterizing transient intermediates in iron metalloenzymes.

Supplementary Material

Refer to Web version on PubMed Central for supplementary material.

Acknowledgements

The authors acknowledge the financial support of this work from U.S. Grants NIH GM 118030 (to J.D.L.) and NIH GM 40392 (to E.I.S.), as well as from the National Research Foundation of Korea (NRF-2018R1C1B6007430 to K.P.). Synchrotron experiments were performed at SPring-8 with the approval of the Japan Synchrotron Radiation Research Institute (JASRI; proposals 2011B1267, 2012A1295, 2013B0105, 2018A0137, 2018B1046, 2018B0137, 2019A1275).

References

(1). Andrews SC The Ferritin-like Superfamily: Evolution of the Biological Iron Storeman from a Rubrerythrin-like Ancestor. Biochim. Biophys. Acta 2010, 1800 (8), 691–705. 10.1016/j.bbagen.2010.05.010. [PubMed: 20553812]

(2). Xing G; Hoffart LM; Diao Y; Prabhu KS; Arner RJ; Reddy CC; Krebs C; Bollinger JM A Coupled Dinuclear Iron Cluster That Is Perturbed by Substrate Binding in Myo-Inositol Oxygenase. Biochemistry 2006, 45 (17), 5393–5401. 10.1021/bi0519607. [PubMed: 16634620]

(3). Hankes LV; Politzer WM; Touster O; Anderson L Myo-Inositol Catabolism in Human Pentosurics: The Predominant Role of the Glucuronate-Xylulose-Pentose Phosphate Pathway. Ann. N. Y. Acad. Sci 1970, 165 (2), 564–576. 10.1111/j.1749-6632.1970.tb56424.x.

(4). Schirmer A; Rude MA; Li X; Popova E; del Cardayre SB Microbial Biosynthesis of Alkanes. Science 2010, 329, 559–562. [PubMed: 20671186]

(5). Fishman A; Tao Y; Bentley WE; Wood TK Protein Engineering of Toluene 4-Monooxygenase of Pseudomonas Mendocina KR1 for Synthesizing 4-Nitrocatechol from Nitrobenzene. Biotechnol. Bioeng 2004, 87 (6), 779–790. 10.1002/bit.20185. [PubMed: 15329936]

(6). Yang B; Hodgkinson A; Millward BA; Demaine AG High Glucose-Induced DNA-Binding Activities of Nuclear Factor of Activated T Cells 5 and Carbohydrate Response Element Binding Protein to the Myo-Inositol Oxygenase Gene Are Inhibited by Sorbinil in Peripheral Blood Mononuclear Cells from Patients with Ty. Int. J. Diabetes Mellit 2010, 2 (3), 169–174. https://doi.org/10.1016/j.ijdm.2010.08.005.

(7). Shao J; Zhou B; Chu B; Yen Y Ribonucleotide Reductase Inhibitors and Future Drug Design. Curr. Cancer Drug Targets 2006, 6 (5), 409–431. [PubMed: 16918309]

(8). Lee SW; Keeney DR; Lim DH; Dispirito AA; Semrau JD Mixed Pollutant Degradation by Methylosinus Trichosporium OB3b Expressing Either Soluble or Particulate Methane Monooxygenase: Can the Tortoise Beat the Hare. Appl. Environ. Microbiol 2006, 72 (12), 7503–7509. 10.1128/AEM.01604-06. [PubMed: 17012599]

(9). Choi YS; Zhang H; Brunzelle JS; Nair SK; Zhao H In Vitro Reconstitution and Crystal Structure of P-Aminobenzoate N-Oxygenase (AurF) Involved in Aureothin Biosynthesis. Proc. Natl. Acad. Sci. U. S. A 2008, 105 (19), 6858–6863. 10.1073/pnas.0712073105. [PubMed: 18458342]

(10). Sazinsky MH; Bard J; Di Donato A; Lippard SJ Crystal Structure of the Toluene/o-Xylene Monooxygenase Hydroxylase from Pseudomonas Stutzeri OX1: Insight Into The Substrate Specificity, Substrate Channeling, And Active Site Tuning Of Multicomponent Monooxygenases. J. Biol. Chem 2004, 279 (29), 30600–30610. 10.1074/jbc.M400710200. [PubMed: 15096510]

(11). Tinberg CE; Lippard SJ Dioxygen Activation in Soluble Methane Monooxygenase. Acc. Chem. Res 2011, 44 (4), 280–288. 10.1021/ar1001473. [PubMed: 21391602]

(12). Austin RN; Chang H; Zylstra GJ; Groves JT The Non-Heme Diiron Alkane Monooxygenase of Pseudomonas Oleovorans (AlkB) Hydroxylates via a Substrate Radical Intermediate. J. Am. Chem. Soc 2000, 122, 11747–11748.

(13). Solomon EI; Park K Structure/Function Correlations over Binuclear Non-Heme Iron Active Sites. J. Biol. Inorg. Chem 2016, 21, 575–588. 10.1007/s00775-016-1372-9. [PubMed: 27369780]

(14). Jasniewski AJ; Que L Dioxygen Activation by Nonheme Diiron Enzymes: Diverse Dioxygen Adducts, High-Valent Intermediates, and Related Model Complexes. Chem. Rev 2018, 118 (5), 2554–2592. 10.1021/acs.chemrev.7b00457. [PubMed: 29400961]

(15). Hanson RS; Hanson TE Methanotrophic Bacteria. Microbiol. Rev 1996, 60 (2), 439–471. [PubMed: 8801441]

(16). Banerjee R; Jones JC; Lipscomb JD Soluble Methane Monooxygenase. Annu. Rev. Biochem 2019, 88 (1), 409–431. 10.1146/annurev-biochem-013118-111529. [PubMed: 30633550]

(17). Fox BG; Froland WA; Dege JE; Lipscomb JD Methane Monooxygenase from Methylosinus Trichosporium OB3b. Purification and Properties of a Three-Component System with High Specific Activity from a Type II Methanotroph. J. Biol. Chem 1989, 264 (17), 10023–10033. [PubMed: 2542319]

(18). Pilkington SJ; Dalton H Soluble Methane Monooxygenase from Methylococcus Capsulatus Bath. Methods Enzymol. 1990, 188, 181–190. 10.1016/0076-6879(90)88032-6.

(19). Lee SK; Nesheim JC; Lipscomb JD Transient Intermediates of the Methane Monooxygenase Catalytic Cycle. J. Biol. Chem 1993, 268 (29), 21569–21577. [PubMed: 8408008]

(20). Liu Y; Nesheim JC; Lee SK; Lipscomb JD Gating Effects of Component B on Oxygen Activation by the Methane Monooxygenase Hydroxylase Component. J. Biol. Chem 1995, 270 (42), 24662–24665. 10.1074/jbc.270.42.24662. [PubMed: 7559577]

(21). Liu KE; Valentine AM; Wang D; Huynh BH; Edmondson DE; Salifoglou A; Lippard SJ Kinetic and Spectroscopic Characterization of Intermediates and Component Interactions in Reactions of Methane Monooxygenase From Methylococcus-Capsulatus (Bath). J. Amer. Chem. Soc 1995, 117 (7), 10174–10185. 10.1021/ja00146a002.

(22). Banerjee R; Meier KK; Münck E; Lipscomb JD Intermediate P* from Soluble Methane Monooxygenase Contains a Diferrous Cluster. Biochemistry 2013, 52 (25), 4331–4342. 10.1021/bi400182y. [PubMed: 23718184]

(23). Lee S-K; Lipscomb JD Oxygen Activation Catalyzed by Methane Monooxygenase Hydroxylase Component: Proton Delivery during the O-O Bond Cleavage Steps. Biochemistry 1999, 38 (14), 4423–4432. 10.1021/bi982712w. [PubMed: 10194363]

(24). Lee S-K; Fox BG; Froland WA; Lipscomb JD; Münck E A Transient Intermediate of Methane Monooygenase Catalytic Cycle Containing an FeIVFeIV Cluster. J. Am. Chem. Soc 1993, 115, 6450–6451. 10.1021/ja00067a086.

(25). Xing G; Diao Y; Hoffart LM; Barr EW; Prabhu KS; Arner RJ; Reddy CC; Krebs C; Bollinger JM Evidence for C-H Cleavage by an Iron-Superoxide Complex in the Glycol Cleavage Reaction Catalyzed by Myo-Inositol Oxygenase. Proc. Natl. Acad. Sci. U. S. A 2006, 103 (16), 6130–6135. 10.1073/pnas.0508473103. [PubMed: 16606846]

(26). Acheson JF; Bailey LJ; Brunold TC; Fox BG In-Crystal Reaction Cycle of a Toluene- Bound Diiron Hydroxylase. Nature 2017, 1–15. 10.1038/nature21681.

(27). Shu L; Nesheim JC; Kauffmann K; Münck E; Lipscomb JD; Que L An Fe2IVO2 Diamond Core Structure for the Key Intermediate Q of Methane Monooxygenase. Science 1997, 275, 515–518. 10.1126/science.275.5299.515. [PubMed: 8999792]

(28). Banerjee R; Proshlyakov Y; Lipscomb JD; Proshlyakov DA Structure of the Key Species in the Enzymatic Oxidation of Methane to Methanol. Nature 2015, 518, 431–434. 10.1038/nature14160. [PubMed: 25607364]

(29). Xue G; Wang D; De Hont R; Fiedler AT; Shan X; Münck E; Que L A Synthetic Precedent for the [FeIV2(Mu-O)2] Diamond Core Proposed for Methane Monooxygenase Intermediate Q. Proc. Natl. Acad. Sci. U. S. A 2007, 104 (52), 20713–20718. 10.1073/pnas.0708516105. [PubMed: 18093922]

(30). Wilkinson EC; Dong Y; Zang Y; Fujii H; Fraczkiewicz R; Fraczkiewicz G; Czernuszewicz RS; Que L Raman Signature of the Fe2O2 “diamond” Core. J. Am. Chem. Soc 1998, 120 (5), 955–962. 10.1021/ja973220u.

(31). Brazeau BJ; Lipscomb JD Kinetics and Activation Thermodynamics of Methane Monooxygenase Compound Q Formation and Reaction with Substrates. Biochemistry 2000, 39, 13503–13515. 10.1021/bi001473l. [PubMed: 11063587]

(32). Nesheim JC; Lipscomb JD Large Kinetic Isotope Effects in Methane Oxidation Catalyzed by Methane Monooxygenase: Evidence for C-H Bond Cleavage in a Reaction Cycle Intermediate. Biochemistry 1996, 35 (31), 10240–10247. 10.1021/bi960596w. [PubMed: 8756490]

(33). Dunietz BD; Beachy MD; Cao Y; Whittington DA; Lippard SJ; Friesner RA Large Scale Ab Initio Quantum Chemical Calculation of the Intermediates in the Soluble Methane Monooxygenase Catalytic Cycle. J. Am. Chem. Soc 2000, 122 (12), 2828–2839. 10.1021/ja9920967.

(34). Basch H; Mogi K; Musaev DG; Morokuma K Mechanism of the Methane → Methanol Conversion Reaction Catalyzed by Methane Monooxygenase: A Density Functional Study. J. Am. Chem. Soc 1999, 121 (31), 7249–7256. 10.1021/ja9906296.

(35). Siegbahn PEM; Crabtree RH; Nordlund P Mechanism of Methane Monooxygenase - A Structural and Quantum Chemical Perspective. J. Biol. Inorg. Chem 1998, 3 (3), 314–317. 10.1007/s007750050238.

(36). Yoshizawa K Two-Step Concerted Mechanism for Methane Hydroxylation on the Diiron Active Site of Soluble Methane Monooxygenase. J. Inorg. Biochem 2000, 78 (1), 23–34. 10.1016/S0162-0134(99)00201-9. [PubMed: 10714702]

(37). Yoshizawa K; Yumura T A Non-Radical Mechanism for Methane Hydroxylation at the Diiron Active Site of Soluble Methane Monooxygenase. Chem. - A Eur. J 2003, 9 (10), 2347–2358. 10.1002/chem.200204269.

(38). Huang S-P; Shiota Y; Yoshizawa K DFT Study of the Mechanism for Methane Hydroxylation by Soluble Methane Monooxygenase (SMMO): Effects of Oxidation State, Spin State, and Coordination Number. Dalt. Trans 2013, 42 (4), 1011–1023. 10.1039/c2dt31304a.

(39). Baik MH; Gherman BF; Friesner RA; Lippard SJ Hydroxylation of Methane by Non-Heme Diiron Enzymes: Molecular Orbital Analysis of C-H Bond Activation by Reactive Intermediate Q. J. Am. Chem. Soc 2002, 124 (49), 14608–14615. 10.1021/ja026794u. [PubMed: 12465971]

(40). Xue G; De Hont R; Münck E; Que L Million-Fold Activation of the [Fe(2)(Micro-O)(2)] Diamond Core for C-H Bond Cleavage. Nat. Chem 2010, 2 (5), 400–405. 10.1038/nchem.586. [PubMed: 20414242]

(41). De Hont RF; Xue G; Hendrich MP; Que L; Bominaar EL; Münck E Mössbauer, Electron Paramagnetic Resonance, and Density Functional Theory Studies of Synthetic S = 1/2 Fe(III)-O-Fe(IV)=O Complexes. Superexchange-Mediated Spin Transition at the Fe(IV)=O Site. Inorg. Chem 2010, 49 (18), 8310–8322. 10.1021/ic100870v. [PubMed: 20795646]

(42). Castillo RG; Banerjee R; Allpress CJ; Rohde GT; Bill E; Que L; Lipscomb JD; DeBeer S, High-Energy-Resolution Fluorescence-Detected X-Ray Absorption of the Q Intermediate of Soluble Methane Monooxygenase. J. Am. Chem. Soc 2017, 139 (49), 18024–18033. 10.1021/jacs.7b09560. [PubMed: 29136468]

(43). Cutsail GE; Banerjee R; Zhou A; Que L; Lipscomb JD; DeBeer S High-Resolution Extended X-Ray Absorption Fine Structure Analysis Provides Evidence for a Longer Fe· · ·Fe Distance in the Q Intermediate of Methane Monooxygenase. J. Am. Chem. Soc 2018, 140, 16807–16820. 10.1021/jacs.8b10313. [PubMed: 30398343]

(44). Sturhahn W Nuclear Resonant Spectroscopy. J. Phys. Condens. Matter 2004, 16 (5), S497–S530. 10.1088/0953-8984/16/5/009.

(45). Seto M; Yoda Y; Kikuta S; Zhang X; Ando M Observation of Nuclear Resonant Scattering Accompanied by Phonon Excitation Using Synchrotron Radiation. Phys. Rev. Lett 1995, 74 (19), 3828–3831. [PubMed: 10058307]

(46). Scheidt WR; Durbin SM; Sage JT Nuclear Resonance Vibrational Spectroscopy--NRVS. J. Inorg. Biochem 2005, 99 (1), 60–71. 10.1016/j.jinorgbio.2004.11.004. [PubMed: 15598492]

(47). Park K; Li N; Kwak Y; Srnec M; Bell CB; Liu LV; Wong SD; Yoda Y; Kitao S; Seto M; Hu M; Zhao J; Krebs C; Bollinger JM; Solomon EI Peroxide Activation for Electrophilic Reactivity by the Binuclear Non-Heme Iron Enzyme AurF. J. Am. Chem. Soc 2017, 139 (20), 7062–7070. 10.1021/jacs.7b02997. [PubMed: 28457126]

(48). Wong SD; Srnec M; Matthews ML; Liu LV; Kwak Y; Park K; Bell CB; Alp EE; Zhao J; Yoda Y; Kitao S; Seto M; Krebs C; Bollinger JM; Solomon EI Elucidation of the Fe(IV)=O

Intermediate in the Catalytic Cycle of the Halogenase SyrB2. Nature 2013, 499 (7458), 320–323. 10.1038/nature12304. [PubMed: 23868262]

(49). Park K; Bell CB; Liu LV; Wang D; Xue G; Kwak Y; Wong SD; Light KM; Zhao J; Alp EE; Yoda Y; Saito M; Kobayashi Y; Ohta T; Seto M; Que L; Solomon EI Nuclear Resonance Vibrational Spectroscopic and Computational Study of High-Valent Diiron Complexes Relevant to Enzyme Intermediates. Proc. Natl. Acad. Sci. U. S. A 2013, 110 (16), 6275–6280. 10.1073/pnas.1304238110. [PubMed: 23576760]

(50). Bell CB; Wong SD; Xiao Y; Klinker EJ; Tenderholt AL; Smith MC; Rohde JU; Que L; Cramer SP; Solomon EI A Combined NRVS and DFT Study of FeIV=O Model Complexes: A Diagnostic Method for the Elucidation of Non-Heme Iron Enzyme Intermediates. Angew. Chemie - Int. Ed 2008, 47 (47), 9071–9074. 10.1002/anie.200803740.

(51). Snyder BER; Böttger LH; Bols ML; Yan JJ; Rhoda HM; Jacobs AB; Hu MY; Zhao J; Ercan Alp E; Hedman B; Hodgson KO; Schoonheydt RA; Sels BF; Solomon EI Structural Characterization of a Non-Heme Iron Active Site in Zeolites That Hydroxylates Methane. Proc. Natl. Acad. Sci. U. S. A 2018, 115 (18), 4565–4570. 10.1073/pnas.1721717115. [PubMed: 29610304]

(52). Valentine AM; Tavares P; Pereira AS; Davydov R; Krebs C; Hoffman BM; Edmondson DE; Boi Hanh Huynh; Lippard SJ Generation of a Mixed-Valent Fe(III)Fe(IV) Form of Intermediate Q in the Reaction Cycle of Soluble Methane Monooxygenase, an Analog of Intermediate X in Ribonucleotide Reductase R2 Assembly. J. Am. Chem. Soc 1998, 120 (9), 2190–2191. 10.1021/ja974169x.

(53). Sturgeon BE; Burdi D; Chen S; Huynh BH; Edmondson DE; Stubbe J; Hoffman BM Reconsideration of X, the Diiron Intermediate Formed during Cofactor Assembly in E. Coli Ribonucleotide Reductase. J. Am. Chem. Soc 1996, 118 (32), 7551–7557. 10.1021/ja960399k.

(54). Lee SJ; McCormick MS; Lippard SJ; Cho U-S Control of Substrate Access to the Active Site in Methane Monooxygenase. Nature 2013, 494 (7437), 380–384. 10.1038/nature11880. [PubMed: 23395959]

(55). Elango NA; Radhakrishnan R; Froland WA; Wallar BJ; Earhart CA; Lipscomb JD; Ohlendorf DH Crystal Structure of the Hydroxylase Component of Methane Monooxygenase from Methylosinus Trichosporium OB3b. Protein Sci. 1997, 6 (3), 556–568. 10.1002/pro.5560060305. [PubMed: 9070438]

(56). Srinivas V; Banerjee R; Lebrette H; Jones JC; Aurelius O; Kim IS; Pham CC; Gul S; Sutherlin KD; Bhowmick A; John J; Bozkurt E; Fransson T; Aller P; Butryn A; Bogacz I; Simon P; Keable S; Britz A; Tono K; Kim KS; Park SY; Lee SJ; Park J; Alonso-Mori R; Fuller FD; Batyuk A; Brewster AS; Bergmann U; Sauter NK; Orville AM; Yachandra VK; Yano J; Lipscomb JD; Kern J; Högbom M High-Resolution XFEL Structure of the Soluble Methane Monooxygenase Hydroxylase Complex with Its Regulatory Component at Ambient Temperature in Two Oxidation States. J. Am. Chem. Soc 2020, 142 (33), 14249–14266. 10.1021/jacs.0c05613. [PubMed: 32683863]

(57). Schulz CE; Castillo RG; Pantazis DA; Debeer S; Neese F Structure-Spectroscopy Correlations for Intermediate Q of Soluble Methane Monooxygenase: Insights from QM/MM Calculations. J. Am. Chem. Soc 2021, 143 (17), 6560–6577. 10.1021/jacs.1c01180. [PubMed: 33884874]

(58). Laurent AD; Jacquemin D TD-DFT Benchmarks: A Review. Int. J. Quantum Chem 2013, 113 (17), 2019–2039. 10.1002/qua.24438.

(59). Sanders-Loehr J; Wheeler WD; Shiemke AK; Averill BA; Loehr TM Electronic and Raman Spectroscopic Properties of Oxo-Bridged Dinuclear Iron Centers in Proteins and Model Compounds. J. Am. Chem. Soc 1989, 111, 8084–8093. 10.1021/ja00203a003.

(60). Gordy W A Relation between Bond Force Constants, Bond Orders, Bond Lengths, and the Electronegativities of the Bonded Atoms. J. Chem. Phys 1946, 14 (5), 305–320. 10.1063/1.1724138.

(61). Brazeau BJ; Wallar BJ; Lipscomb JD Unmasking of Deuterium Kinetic Isotope Effects on the Methane Monooxygenase Compound Q Reaction by Site-Directed Mutagenesis of Component B. J. Am. Chem. Soc 2001, 123 (42), 10421–10422. 10.1021/ja016632i. [PubMed: 11604007]

(62). Matthews ML; Krest CM; Barr EW; Vaillancourt H; Walsh CT Substrate-Triggered Formation and Remarkable Stability of the C-H Bond-Cleaving Chloroferryl Intermediate in the

Aliphatic Halogenase, SyrB2. Biochemistry 2009, 48, 4331–4343. 10.1021/bi900109z. [PubMed: 19245217]

(63). Zaragoza JPT; Siegler MA; Goldberg DP A Reactive Manganese(IV)-Hydroxide Complex: A Missing Intermediate in Hydrogen Atom Transfer by High-Valent Metal-Oxo Porphyrinoid Compounds. J. Am. Chem. Soc 2018, 140 (12), 4380–4390. 10.1021/jacs.8b00350. [PubMed: 29542921]

(64). Siegbahn PEM O-O Bond Cleavage and Alkane Hydroxylation in Methane Monooxygenase. J. Biol. Inorg. Chem 2001, 6 (1), 27–45. 10.1007/s007750000184. [PubMed: 11191221]

(65). Baik MH; Newcomb M; Friesner RA; Lippard SJ Mechanistic Studies on the Hydroxylation of Methane by Methane Monooxygenase. Chem. Rev 2003, 103 (6), 2385–2419. 10.1021/cr950244f. [PubMed: 12797835]

(66). Gherman BF; Dunietz BD; Whittington DA; Lippard SJ; Friesner RA Activation of the C-H Bond of Methane by Intermediate Q of Methane Monooxygenase: A Theoretical Study. J. Am. Chem. Soc 2001, 123 (16), 3836–3837. 10.1021/ja0055108. [PubMed: 11457123]

(67). Gherman BF; Lippard SJ; Friesner RA Substrate Hydroxylation in Methane Monooxygenase: Quantitative Modeling via Mixed Quantum Mechanics/Molecular Mechanics Techniques. J. Am. Chem. Soc 2005, 127 (3), 1025–1037. 10.1021/ja049847b. [PubMed: 15656641]

(68). Musaev DG; Basch H; Morokuma K Theoretical Study of the Mechanism of Alkane Hydroxylation and Ethylene Epoxidation Reactions Catalyzed by Diiron Bis-Oxo Complexes. The Effect of Substrate Molecules. J. Am. Chem. Soc 2002, 124 (15), 4135–4148. 10.1021/ja0176393. [PubMed: 11942853]

(69). Baldwin MJ; Roo DE; Pate JE; Fujisawa K; Kitajima N; Solomon EI Spectroscopic Studies of Side-On Peroxide-Bridged Binuclear Copper(II) Model Complexes of Relevance to Oxyhemocyanin and Oxytyrosinase. J. Am. Chem. Soc 1992, 114 (26), 10421–10431. 10.1021/ja00052a043.

(70). Dassama LMK; Silakov A; Krest CM; Calixto JC; Krebs C; Bollinger JM; Green MTA 2.8 Å Fe—Fe Separation in the Fe2 III/IV Intermediate, X, from Escherichia Coli Ribonucleotide Reductase. J. Am. Chem. Soc 2013, 135, 16758–16761. [PubMed: 24094084]

(71). Schulz CE; Castillo RG; Pantazis DA; Debeer S; Neese F Structure – Spectroscopy Correlations for Intermediate Q of Soluble Methane Monooxygenase : Insights from QM / MM Calculations. 2021. 10.1021/jacs.1c01180.

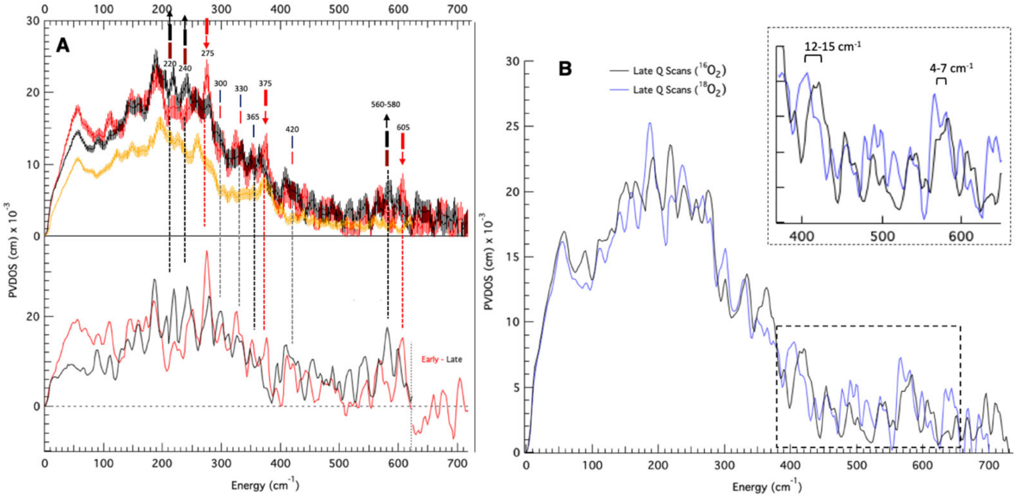

Figure 1.

NRVS spectra of Q samples indicating time-dependent changes in the beam and isotopic perturbations. (A) Top: NRVS spectra (including error) of early Q (hours 1-15; top red), and late decay scans (30+ hours; top black), and $MMOH_{red}$ (multiplied by 0.5; top orange). Late decay scans include $^{16}O_2$ and $^{18}O_2$ data in order to maximize S/N. At the top of the figure, thick red lines indicate major features of early Q data. Brown lines indicate features which grow in over two phases. Black thick lines indicate major features of decayed Q data. Thin red and black lines indicate features shared by both early and decayed Q data. Bottom: $MMOH_{red}$-subtracted and renormalized spectra (Q red and decay black). In the bottom plot, based on poor S/N the intermediate Q and decay spectra past 620 cm^{-1} are given as Early – Late scan data (no feature above noise is observed). (B) NRVS spectra of $^{16}O_2$ (71 scans) and $^{18}O_2$ (110 scans, with data accumulated at ~ 1/2 count rate as $^{16}O_2$ decay data) labeled Q after 30+ hours of measurement.

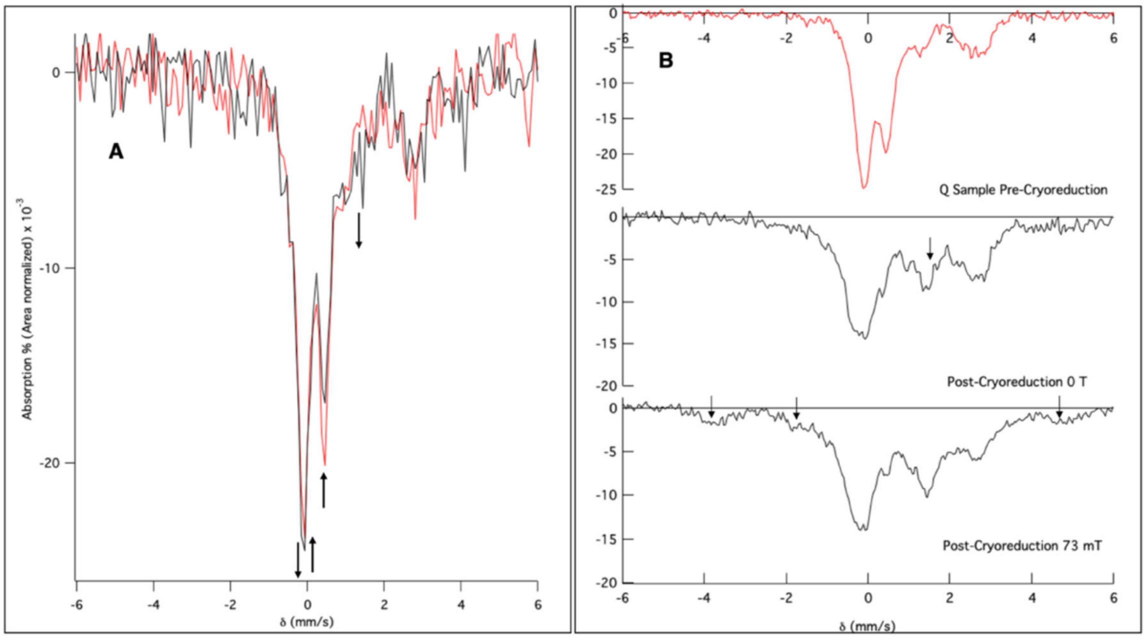

Figure 2.

Mössbauer spectra collected at 6 K of intermediate Q exposed to the NRVS X-ray beam and to cryoreduction. (A) Mössbauer spectra before (red) and after (black) NRVS measurement of Q. Arrows indicate major changes pre- and post-NRVS measurement. (B) Mössbauer spectra of a Q sample irradiated to 6 Mrad (top to middle). Arrow in the middle spectrum indicates a new feature present after cryoreduction. Bottom spectrum post-cryoreduction in an applied 73 mT parallel field showing the appearance of paramagnetic features (arrows).

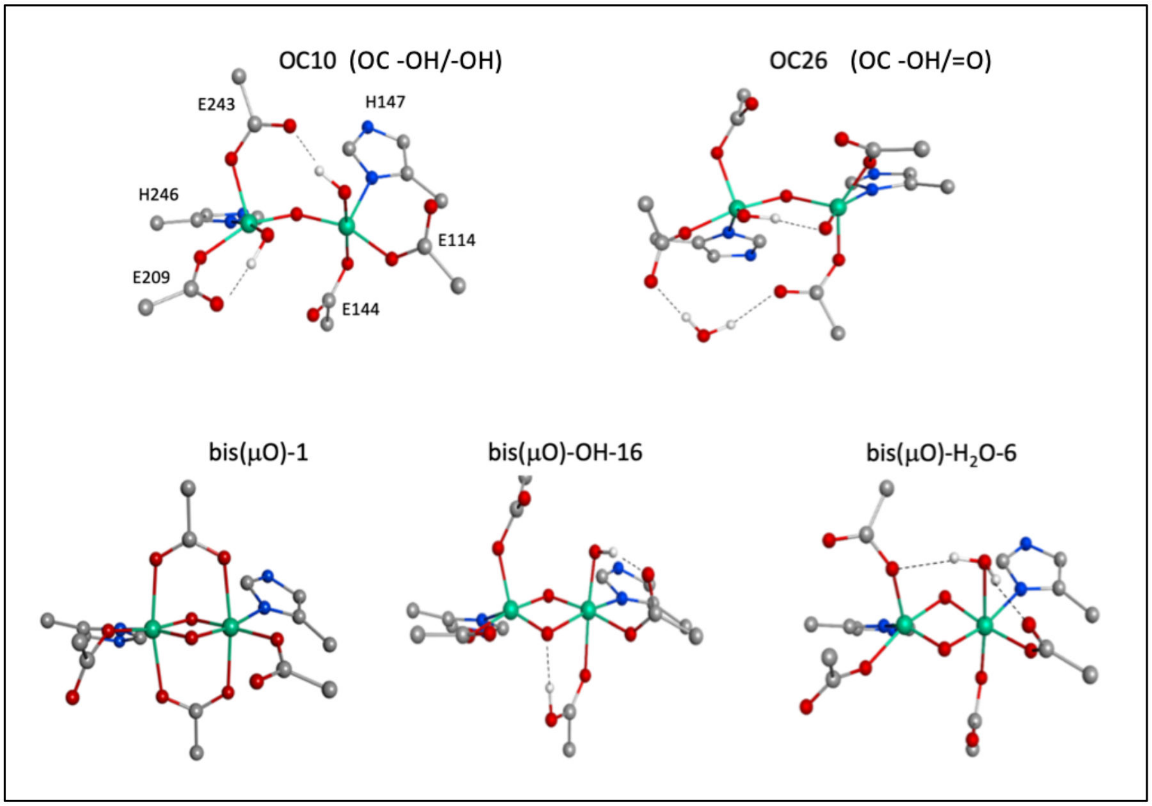

Figure 3.

Structural model subtypes for Q. Includes structural representatives for the OC -OH/-OH (**OC10**), OC -OH/=O (**OC26**) subclasses at the top, and bis(μO) (**bis(μO-1)**), bis(μO)-OH (**bis(μO)-OH-16**), and bis(μO)-H_2O (**bis(μO)-H_2O-6**) subclasses at the bottom.

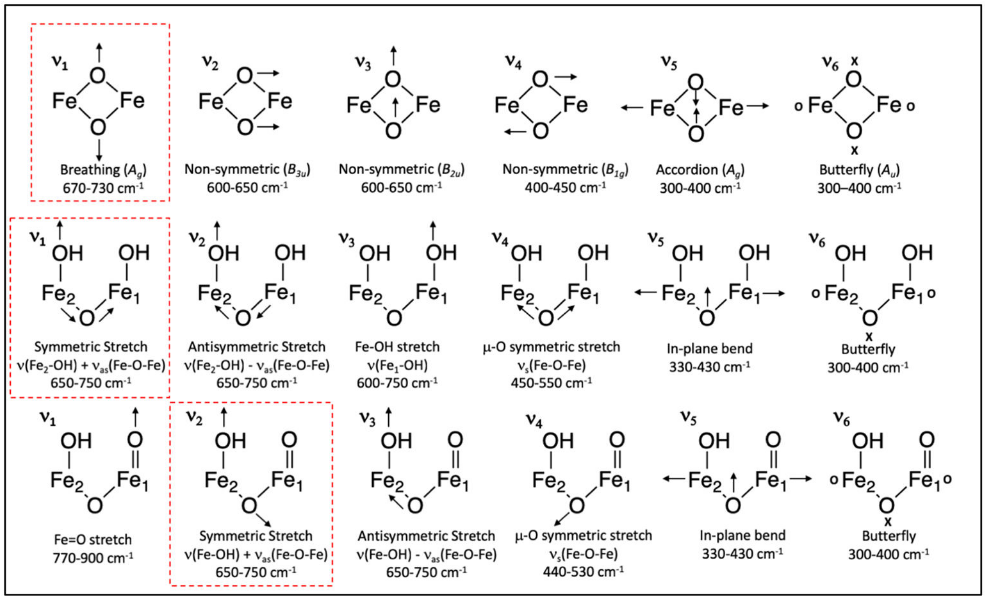

Figure 4.

Normal modes for the Q closed core bis(μO), bis(μO)-OH, and bis(μO)-H_2O subclasses (top), and Q open core OC -OH/-OH (middle) and OC -OH/=O subclasses (bottom). Closed core modes defined in D_{2h} symmetry. The calculated vibration in each of these models that corresponds to the reported rR 690 cm^{-1} vibration is highlighted in red. Arrows denote in-plane motion, and “x” and “o” characters denote out-of-plane motions.

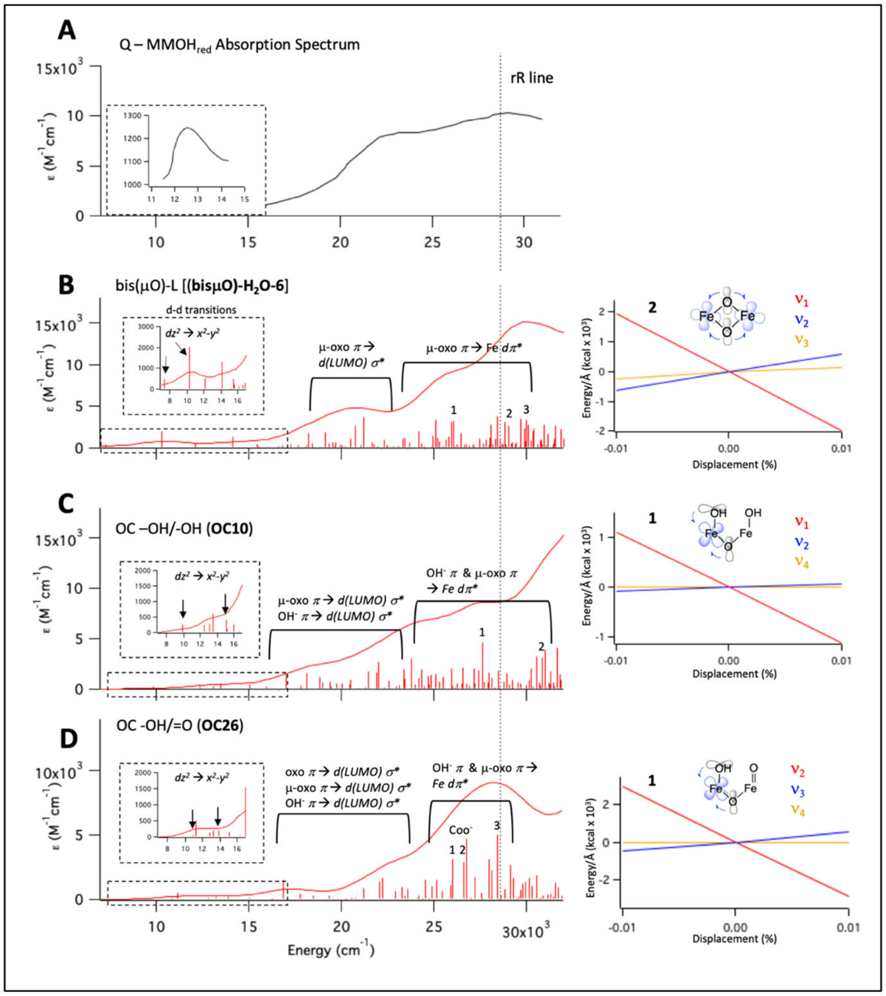

Figure 5.

Q UV-vis absorption spectrum and TD-DFT calculated spectra and predicted rR enhancement of Q models. (A) Experimental absorption spectrum for intermediate Q. Inset: expanded scale for low energy region. Adapted from reference 16. (B) TD-DFT spectrum (calculated using CAM-B3LYP, downshifted by 3,000 cm^{-1} based on calibration in Figure S14), left, of bis(μO)-H$_2$O-6 as representative of the bis(μO)-L (L = OH$^-$, H$_2$O, or vacant site) models. A qualitative description of transition 2 is shown on the right, along with the LCT for transition 2 calculated for modes ν_1, ν_2, and ν_3 (Figure 4 top). (C) TD-DFT calculated spectrum (left) of OC10 as a representative spectrum of the OC -OH/-OH models. A qualitative depiction of transition 1 is given on the right, along with the LCTs for transition 1 along modes ν_1, ν_2, and ν_4 (Figure 4, middle). (D) TD-DFT spectrum (left) of OC26 as representative of the OC -OH/=O models. Transition 1 is schematically given on the right, along with LCTs for transition 1 for modes ν_2, ν_3, and ν_4 (Figure 4, bottom).

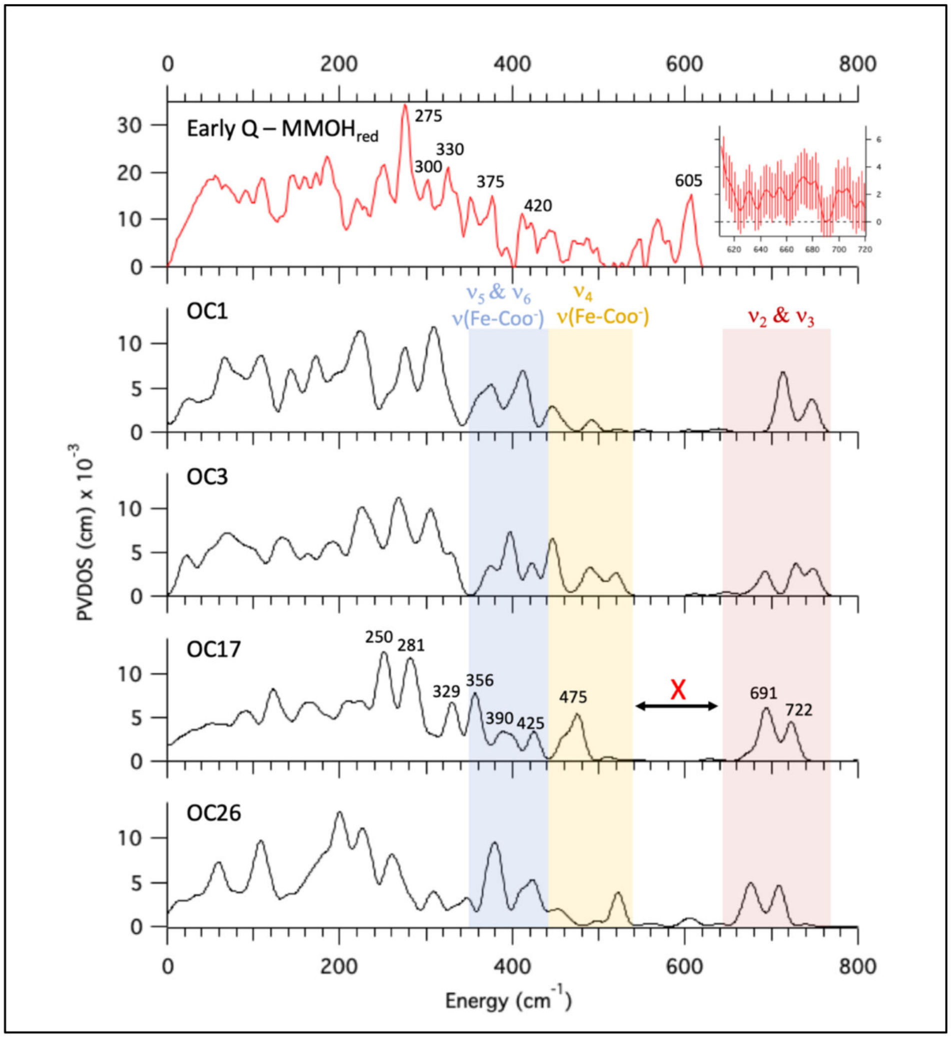

Figure 6.

Correlation of OC -OH/=O computed NRVS spectra to experimental data. The Q – MMOH$_{red}$ (and renormalized) PVDOS spectrum is shown at top in red (adapted from Figure 1A, bottom). Q data (unsubtracted including error) between 610 and 720 cm^{-1} are provided in the top right inset. OC -OH/=OH models that possess a ν_2 mode (see Figure 4, bottom) with the approximate 690 cm^{-1} mixed isotope signal are shown below in black (**OC1**, **OC3**, **OC17**, **OC26**. Their structures are given in Table S1). The blue region indicates low energy bending modes (ν_5 & ν_6 Figure 4 bottom) and terminal ν(Fe-COO$^-$) stretches. The yellow region also contains ν(Fe-COO$^-$) stretches and the ν_s(Fe-O-Fe) mode (ν_4 Figure 4, bottom). The red region contains ν_2 and its antisymmetric pair (ν_3 Figure 4, bottom).

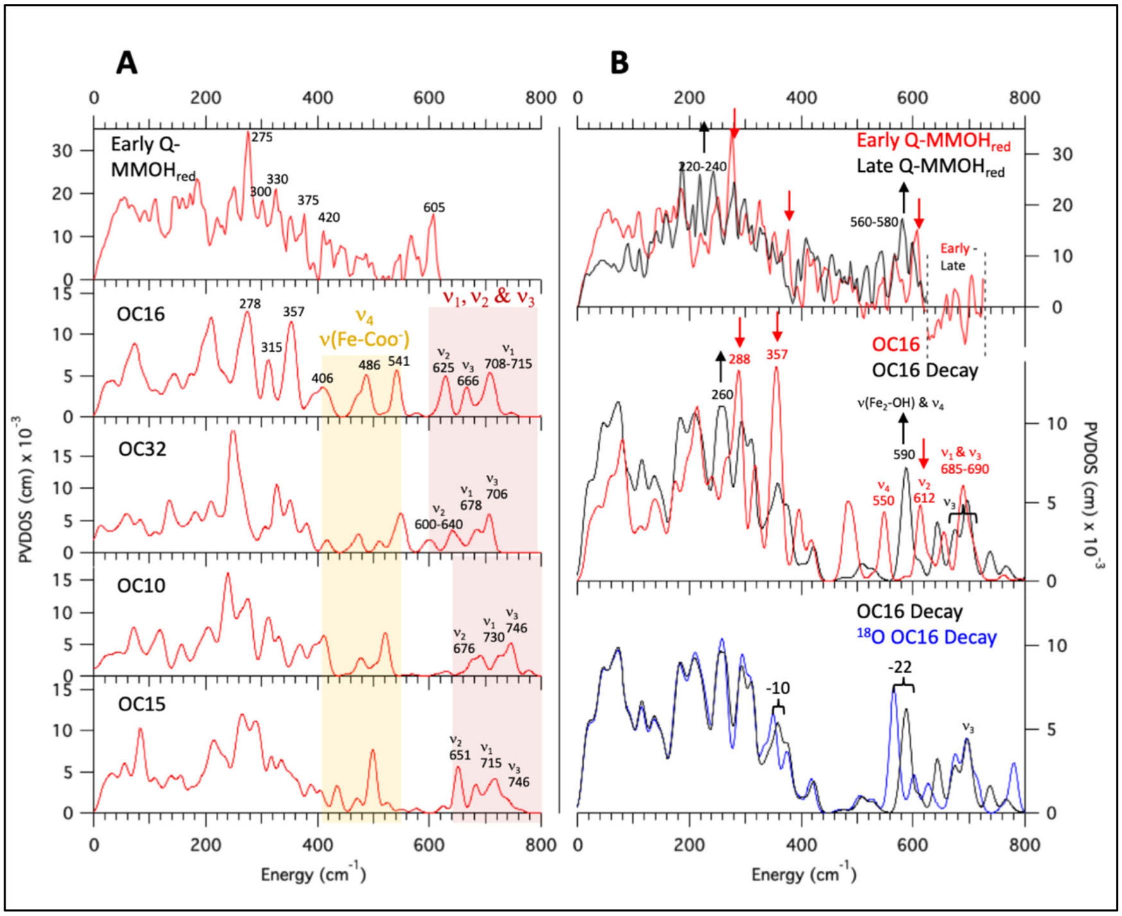

Figure 7.

NRVS spectra of OC -OH/-OH models and the cryoreduction decay spectra for **OC16**. (A) Early Q – MMOH$_{red}$ NRVS data (top), with calculated spectra given below for the four OC -OH/-OH models possessing a ν_1 mode (Figure 4 middle) with appropriate $^{16}O^{18}O$ mixed isotope and deuterium isotope effects (calculated with BP86 and 10% HF). Yellow region contains the ν_4 (Figure 4 middle) and terminal ν(Fe-COO$^-$) modes. Red region contains the ν_1, ν_2, and ν_3 modes (Figure 4). (B) Top: Early Q – MMOH$_{red}$ (red spectrum) and Decayed Q – MMOH$_{red}$ (black spectrum) NRVS data, with arrows highlighting changes in the spectra from early to late scans. Middle: NRVS spectrum for the B3LYP DFT-optimized **OC16** model (red; see Figure S25 for the close correlation of NRVS calculations between B3LYP vs. 10% HF in BP86), as well the calculated decay spectrum (**OC16 Decay**) consisting of a 40%/60% mixture of its Fe$_2$(III)Fe$_1$(IV) and Fe(III)$_2$ optimized calculated NRVS spectra, respectively (black). Arrows indicate major changes from **OC16** to **OC16 Decay**. Bottom: Calculated NRVS spectra for the **OC16 Decay** from Figure 7B middle (black) and its $^{18}O_2$ labeled isotopomer (**$^{18}O_2$ OC16 Decay**, blue).

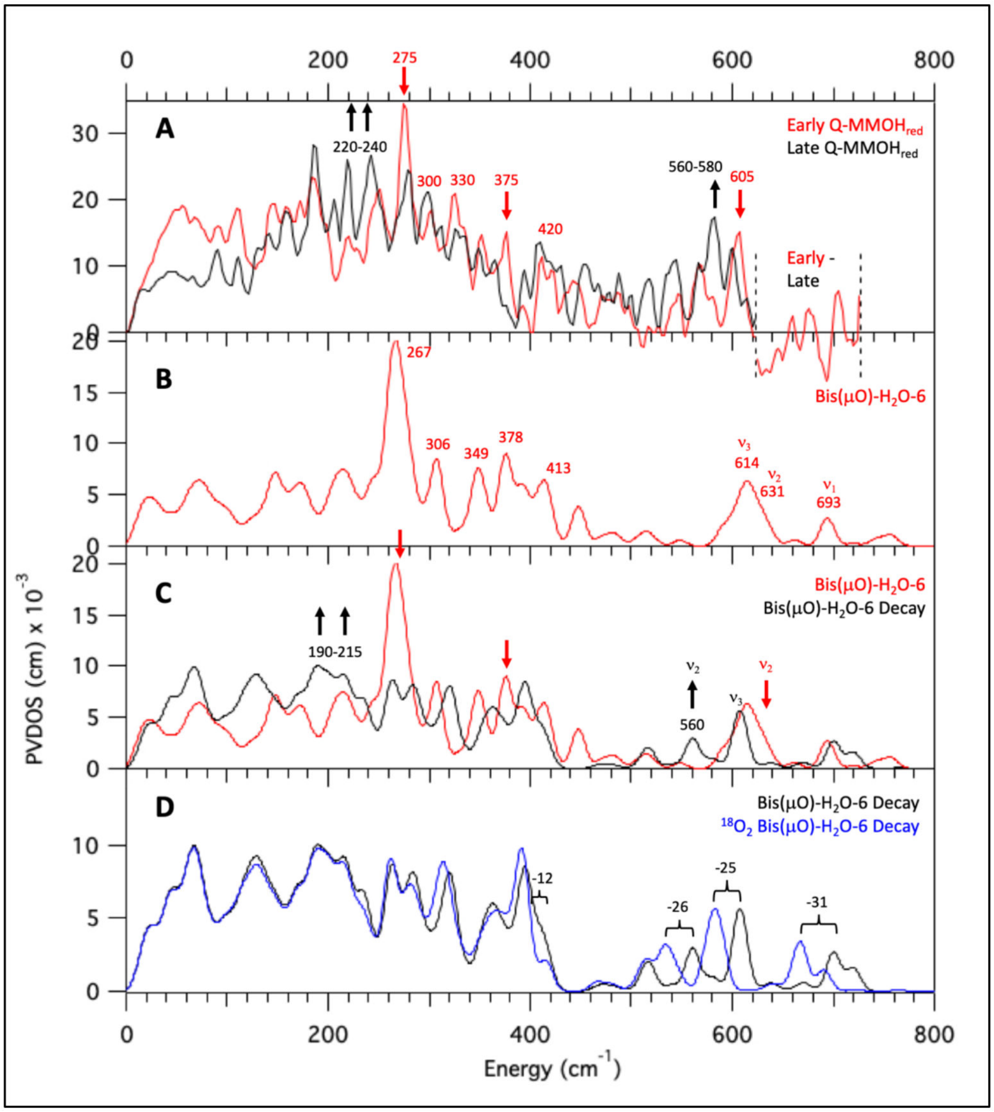

Figure 8.

Calculated NRVS spectra of **bis(μO)-H_2O-6** as representative of bis(μO) and bis(μO)-H_2O subclasses. All spectra simulated with B3LYP. (A) Early Q – MMOH$_{red}$ (red) and Decayed Q – MMOH$_{red}$ (black) NRVS data. Arrows indicate major spectral differences. (B) Calculated NRVS spectrum of **bis(μO)-H_2O-6**. (C) Calculated NRVS spectra **bis(μO)-H_2O-6** (red) and its simulated decay product **bis(μO)-H_2O-6 Decay** (black). Arrows indicate major spectral differences. (D) Calculated NRVS spectra for **bis(μO)-H_2O-6 Decay** (black) and its $^{18}O_2$ isotopomer (blue).

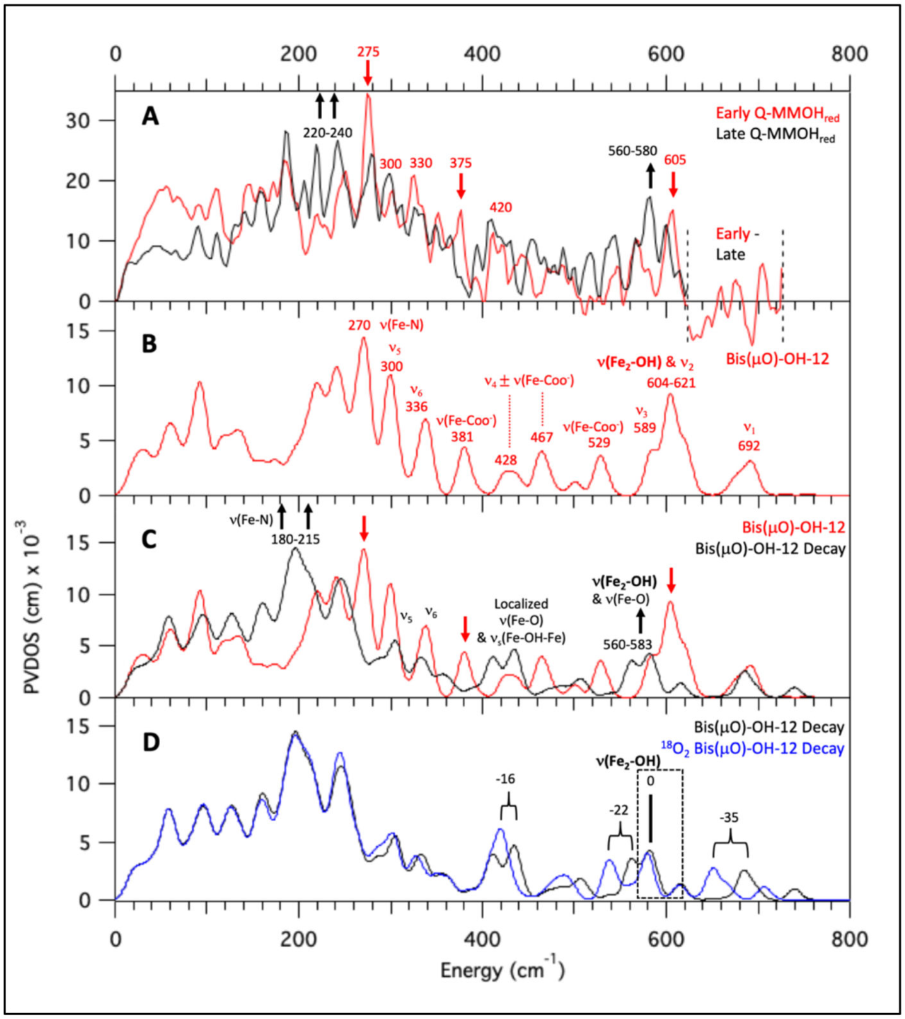

Figure 9.

Calculated NRVS spectra of **bis(μO)-OH-12** as representative of the bis(μO)-OH subclass. All spectra simulated with B3LYP. (A) Early Q – MMOH$_{red}$ (red) and Decayed Q – MMOH$_{red}$ (black) NRVS data. Arrows indicate major spectral differences. (B) Calculated NRVS spectrum of **bis(μO)-OH-12**. (C) Calculated NRVS spectra for **bis(μO)-OH-12** (red) and its simulated cryoreduced product (**bis(μO)-OH-12 Decay** in black; see text for details). Arrows indicate major spectral differences. (D) Calculated NRVS spectra for **bis(μO)-OH-12 Decay** (black) and its $^{18}O_2$ isotopomer (blue).

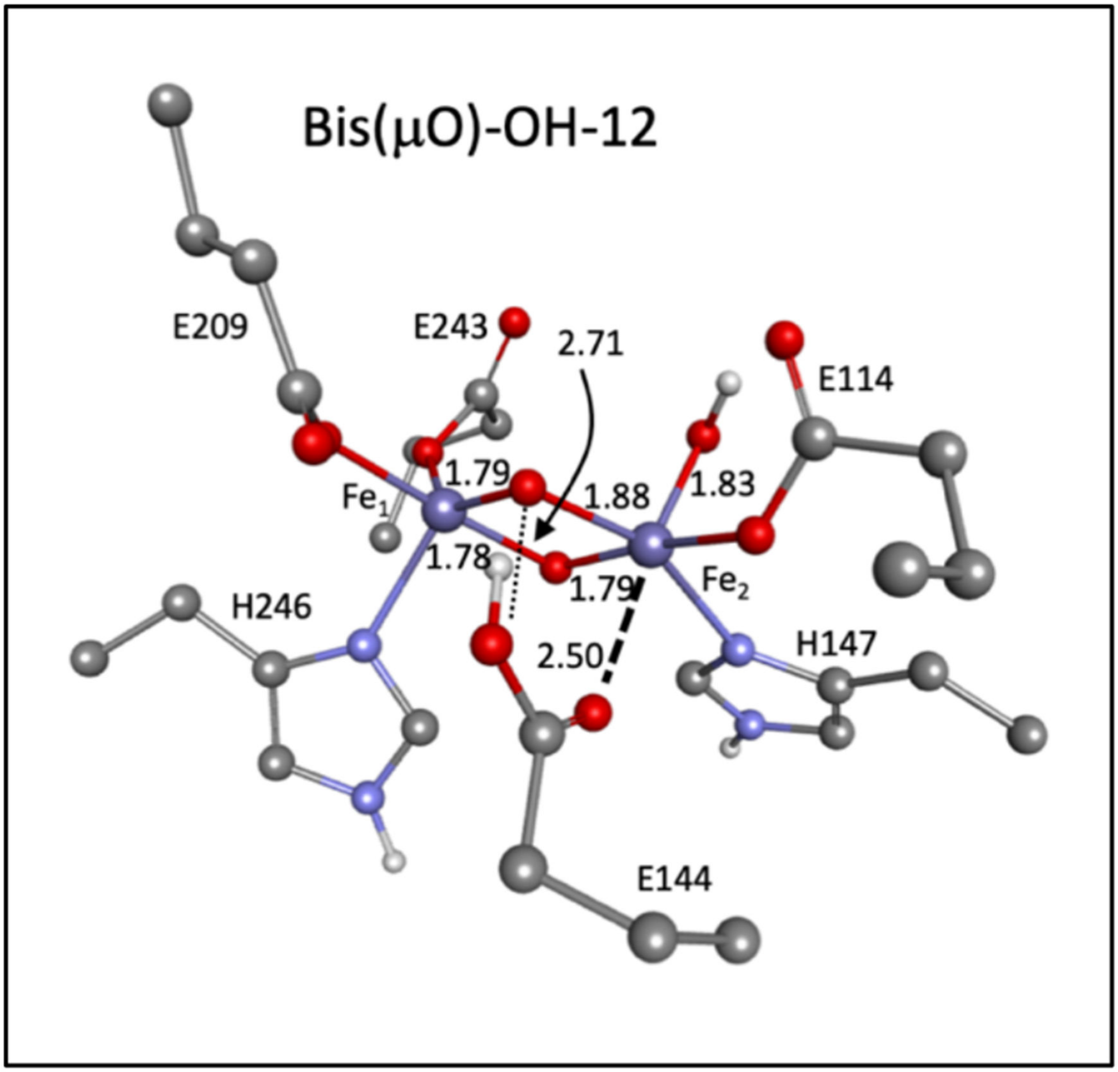

Figure 10.

Structure for **bis(μO)-OH-12**.

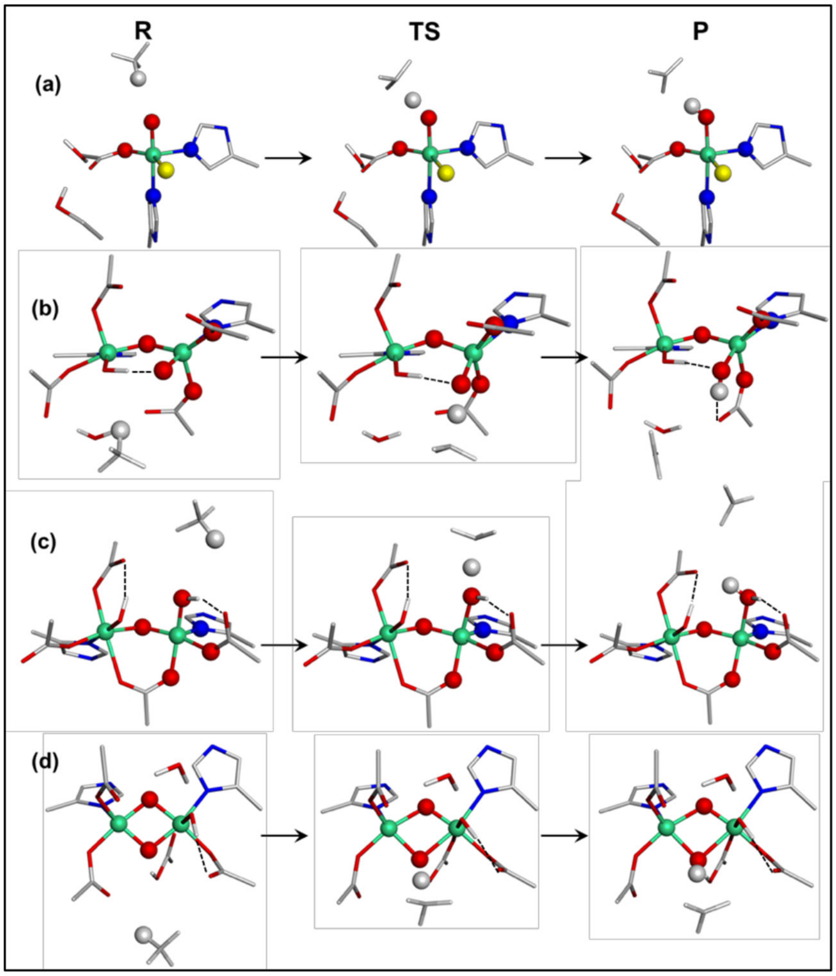

Figure 11.

Reaction coordinates calculated for hydrogen atom abstraction from methane by (a) the mononuclear Fe(IV)=O site in SyrB2, (b) the open core HO-Fe(IV)-μO-Fe(IV)=O site in **OC26**, (c) the open-core HO-Fe(IV)-μO-Fe(IV)-OH site in **OC15**, and (d) the closed core bis(μO)-bridged $Fe(IV)_2$ site in **bis(μO)-OH12**. The Fe, C, N, O, Cl, and H atoms are displayed in green, gray, blue, red, yellow, and white, respectively.

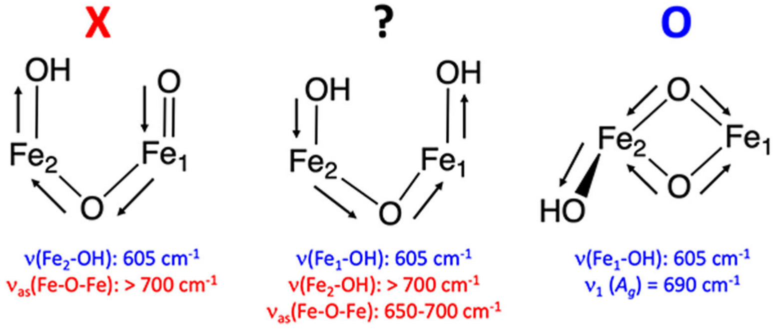

Figure 12.

Representation of the ligand donations required to produce a 605 cm^{-1} NRVS feature in the OC -OH/=O (left), OC -OH/-OH (middle), and bis(μO)-OH (right) subclasses. The direction of donation is symbolized with arrows. In the OC subclasses, the donation required to create a long Fe-OH bond to reproduce the low ν(Fe-OH) 605 cm^{-1} NRVS feature of Q results in the absence of a ν(Fe-OH) + ν_{as}(Fe-O-Fe) symmetric mode that would be assigned to the rR feature at 690 cm^{-1}. In the bis(μO)-OH subclass, the (μ-O)$_2$ core provides strong donation to facilitate a long Fe$_2$-OH bond and thus a ν(Fe$_2$-OH) mode near 605 cm^{-1}, and the A_g breathing mode (ν_1 Figure 4) satisfies the 690 cm^{-1} rR assignment.

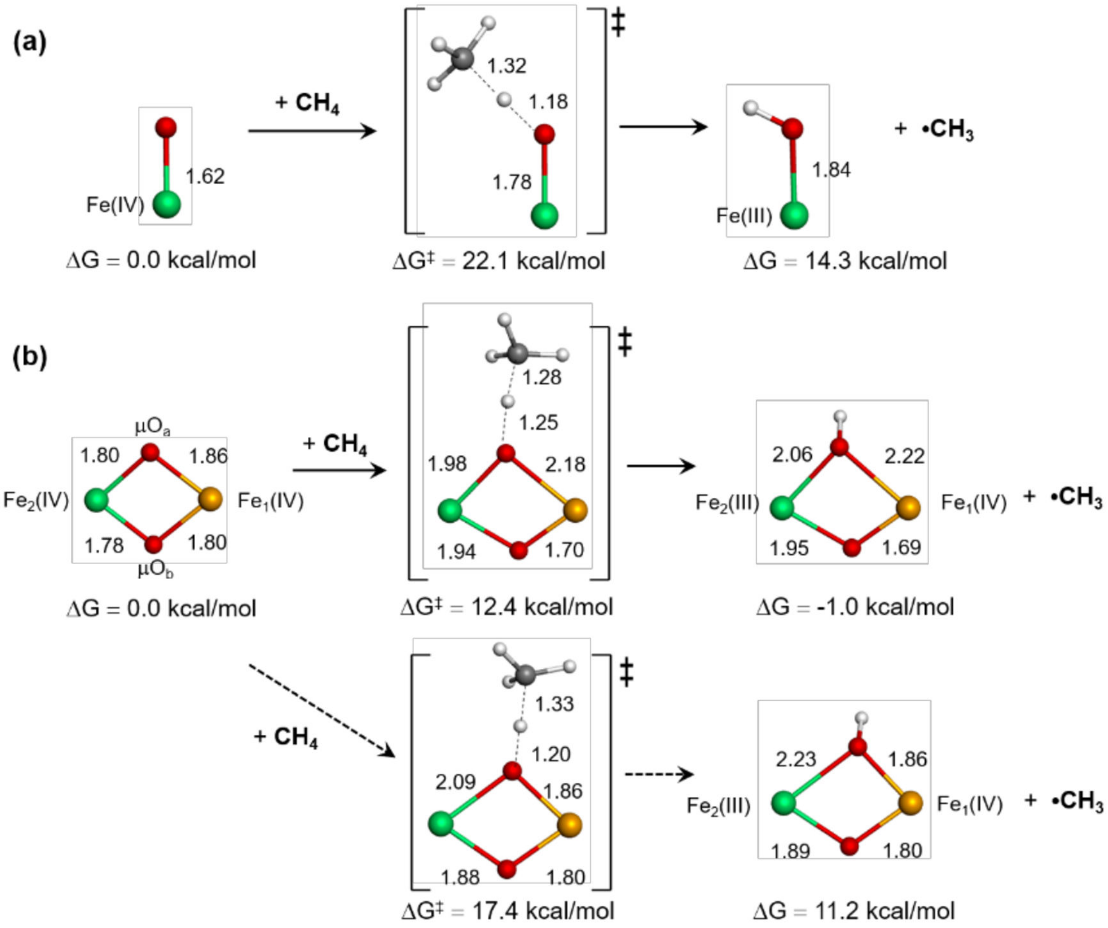

Figure 13.

H atom abstraction from CH_4 by (a) the mononuclear Fe(IV)=O system and **(b)** the binuclear closed-core $Fe_2(\mu O)_2$ system with (top) and without (core frozen, bottom) the bis(μO) concerted motions. The electron-accepting Fe centers are displayed in green, while the redox-neutral Fe center is colored in orange.

Table 1.

Potential energy, enthalpy, and free energy changes and intrinsic barriers (in kcal/mol) involved in hydrogen atom abstraction from methane by models in Figure 11

Systems	ΔE; ΔH; ΔG	$\Delta E^{\ddagger}$; $\Delta H^{\ddagger}$; $\Delta G^{\ddagger}$	$\Delta E^{\ddagger}_{int}$; $\Delta H^{\ddagger}_{int}$; $\Delta G^{\ddagger}_{int}$
Fe(IV)=O	17.1; 14.7; 14.3	25.1; 20.1; 22.1	15.3; 11.6; 14.0
HO-Fe(IV)-μO-Fe(IV)=O	10.8; 7.2; 10.4	24.8; 19.7; 25.0	19.0; 15.9; 19.4
HO-Fe(IV)-μO-Fe(IV)-OH	0.7; −0.3; −2.1	19.8; 14.8; 15.4	19.4; 14.9; 16.4
Fe(IV)-(μO)$_2$-Fe(IV)-OH [**]	3.6; 2.1; −1.0	15.7; 11.2; 12.4	13.9; 10.1; 12.9

[*] ΔG values are calculated at 5 °C.

[**] ΔG and

[‡] ΔG values for Fe(IV)-(μO)$_2$-Fe(IV)-OH$_2$ are 3.1 and 11.1 kcal/mol.